

A family of high-order gas-kinetic schemes and its comparison with Riemann solver based high-order methods

Xing Ji ^a, Fengxiang Zhao ^c, Wei Shyy ^b, Kun Xu ^{a,b,*}

^a Department of Mathematics, Hong Kong University of Science and Technology, Clear Water Bay, Kowloon, Hong Kong

^b Department of Mechanical and Aerospace Engineering, Hong Kong University of Science and Technology, Clear Water Bay, Kowloon, Hong Kong

^c Institute of Applied Physics and Computational Mathematics, Beijing, China

ARTICLE INFO

Article history:

Received 31 July 2017

Received in revised form 17 November 2017

Accepted 29 November 2017

Available online 5 December 2017

Keywords:

Gas-kinetic scheme

Multi-stage and multi-derivative methods

Euler equations

Navier–Stokes equations

ABSTRACT

Most high order computational fluid dynamics (CFD) methods for compressible flows are based on Riemann solver for the flux evaluation and Runge–Kutta (RK) time stepping technique for temporal accuracy. The advantage of this kind of space–time separation approach is the easy implementation and stability enhancement by introducing more middle stages. However, the n th-order time accuracy needs no less than n stages for the RK method, which can be very time and memory consuming due to the reconstruction at each stage for a high order method. On the other hand, the multi-stage multi-derivative (MSMD) method can be used to achieve the same order of time accuracy using less middle stages with the use of the time derivatives of the flux function. For traditional Riemann solver based CFD methods, the lack of time derivatives in the flux function prevents its direct implementation of the MSMD method. However, the gas kinetic scheme (GKS) provides such a time accurate evolution model. By combining the second-order or third-order GKS flux functions with the MSMD technique, a family of high order gas kinetic methods can be constructed. As an extension of the previous 2-stage 4th-order GKS, the 5th-order schemes with 2 and 3 stages will be developed in this paper. Based on the same 5th-order WENO reconstruction, the performance of gas kinetic schemes from the 2nd- to the 5th-order time accurate methods will be evaluated. The results show that the 5th-order scheme can achieve the theoretical order of accuracy for the Euler equations, and present accurate Navier–Stokes solutions as well due to the coupling of inviscid and viscous terms in the GKS formulation. In comparison with Riemann solver based 5th-order RK method, the high order GKS has advantages in terms of efficiency, accuracy, and robustness, for all test cases. The 4th- and 5th-order GKS have the same robustness as the 2nd-order scheme for the capturing of discontinuous solutions. The current high order MSMD GKS is a multi-dimensional scheme with incorporation of both normal and tangential spatial derivatives of flow variables at a cell interface in the flux evaluation. The scheme can be extended straightforwardly to viscous flow computation in unstructured mesh. It provides a promising direction for the development of high-order CFD methods for the computation of complex flows, such as turbulence and acoustics with shock interactions.

© 2017 Elsevier Inc. All rights reserved.

* Corresponding author at: Department of Mathematics, Hong Kong University of Science and Technology, Clear Water Bay, Kowloon, Hong Kong.
E-mail addresses: xjiad@connect.ust.hk (X. Ji), kobezhao@126.com (F. Zhao), weishyy@ust.hk (W. Shyy), makxu@ust.hk (K. Xu).

1. Introduction

The flux of the gas kinetic scheme (GKS) is based on a time-dependent evolution solution of the kinetic equation, such as the Bhatnagar–Gross–Krook (BGK) model [3]. It targets on the Euler and NS solutions [47,51]. In comparison with traditional Riemann solver based CFD methods, the distinguishable points of GKS include the followings. Firstly, the time evolving gas distribution function provides a multiple scale flow physics from the kinetic particle transport to the hydrodynamic wave propagation [50]. The particle transport from the initial discontinuity supplies numerical dissipation in the discontinuous region and the wave propagating solution from the equilibrium state provides accurate solution in the smooth region. The multiple scale nature of the flux function bridges the evolution from the upwind flux vector splitting to the central difference Lax–Wendroff type discretization, where both inviscid and viscous fluxes are obtained from the moments of a single gas distribution function [47,51,48]. Secondly, the GKS is intrinsically a multi-dimensional scheme, where both normal and tangential derivatives of flow variables around a cell interface participate the time evolution of the gas distribution function [51]. The hyperbolic kinetic equation with local relaxation provides a compact physical domain for the design of the numerical schemes in comparison with the direct solvers of the Navier–Stokes equations. The numerical solutions in GKS are not sensitive to the mesh distributions due to the absence of direct explicit evaluation of dissipative terms. Thirdly, the time dependent flux function achieves higher order time accuracy than that in the Riemann flux. A one-step 3rd-order scheme can be directly constructed [27]. Fourthly, a unified GKS (UGKS) can be developed for multi-scale gas dynamics [49,50].

The second order schemes were mostly developed in 1980s and they are the main numerical schemes used in engineering applications. Great efforts have been paid on the development of high order (3rd order or higher) methods in the past decades, which are expected to provide more accurate solutions with less computational cost than second order methods [46]. It is still early to point out the appropriate approaches for high order schemes, especially for high speed compressible flow with discontinuities. There are many attempts in the construction of high order schemes, such as the k-exact [2], weighted essentially non-oscillatory (WENO) [23,4,1,54], multi-moment constrained (MCV) methods [20], discontinuous Galerkin (DG) [7], flux reconstruction approach [19], and many others. Most approaches are focusing on high order initial reconstruction, which achieves high order accuracy in smooth region and avoids oscillation in the discontinuous region. In terms of evolution model, same as the second order schemes, the Riemann solver is commonly used for the flux evaluation [45]. In order to improve the time accuracy, the traditional Runge–Kutta (RK) time-stepping method is used [21]. The RK methods separate the spatial and temporal discretization, which could improve the stability for hyperbolic problems in comparison with the single stage or the Adams family of methods under the same reconstruction [15,16]. The RK method can be used in GKS as well under FV or DG frameworks [41,37,36]. However, the n th-order accuracy in RK method requires no less than n stages. For a classical 4th-order RK method, we need 4 stages. While for a 5th-order RK method, usually 6 stages are needed [12]. For a high order scheme, the initial reconstruction for the middle stages may take most of the computational time. All those are related to the use of Riemann solver, which may be the real barrier for the development of efficient high order schemes.

On the other hand, the GKS is based on the high order gas evolution model, which provides time-dependent flux function. The second and third order schemes can be developed through a single updating step without middle stages [27]. With the 5th-order WENO reconstruction, a 3rd order GKS has been developed for both 2D and 3D inviscid and viscous flow computations [29,33]. A compact 3rd-order scheme in structured and unstructured meshes has been developed as well [32,34]. Although the 3rd-order GKS flux function takes approximately 4 to 6 times of the computational time of a 2nd order GKS flux, the one step method still shows high efficiency against a 3 stages RK method, since the spatial reconstructions take a significant amount of CPU time. One step high order schemes have been developed under ADER framework as well, which utilizes the hyperbolic Riemann problem for the advection of the higher order DERivatives [42,44,9], where not only one but all time derivatives up to order N -th order can be obtained either via Taylor series expansions and the Cauchy–Kowalewskaya procedure or via a weak form of the governing PDE in space and time. Since the 3rd-order GKS flux function depends on the initial reconstructions of derivatives, such as 1st, 2nd, and 3rd-order ones, which become more and more unreliable for the higher order derivatives, especially in the discontinuous regions, the one step 3rd-order GKS becomes less robust than the second order scheme. Instead of constructing high order one step GKS methods, it may become a good choice to combine the advantages of both time accuracy of GKS flux function and RK technique for the robustness.

Starting from 1940s, methods with multiple stages and multiple derivatives (MSMD) have been used for numerical solution of ODEs [30]. This group of methods was reviewed and defined by Hairer and Wanner [17]. The MSMD including 2nd-order derivatives was studied up to 7th-order accuracy for explicit and semi-implicit methods [14] and was compared with RK methods [5]. This technique has been successfully applied for oscillatory differential equations [10] and the Schrödinger equation [11] in ODE region. After realizing the benefits from the MSMD, it has been firstly adopted to explicit finite difference and DG solvers [40]. Then, remarkable work has been done for the implementation of implicit MSMD [22, 39]. To further improve the robustness of MSMD for hyperbolic problems, the strong stability preserving (SSP) theory was developed for two-derivative multi-stage methods recently and a 6th-order SSP MSMD has been presented [38]. Almost at the same period, a 4th-order 2 stages scheme based on the generalized Riemann problem (GRP) for the Euler equations has been proposed [26]. Similarly, a 4th-order 2 stages GKS has been designed for the Navier–Stokes solutions [35]. Benefiting from the 2nd-order GKS flux function and two stages strategy, the 4th-order 2 stages GKS shows great accuracy and out-

standing robustness. Due to the absence two reconstructions, the efficiency of the scheme is superior in comparison with other Riemann solver based 4th-order schemes with 4 stages RK technique.

In this paper, two kinds of 5th-order GKS will be proposed by using MSMD technique and taking the advantages of high order time-accurate GKS flux function. One of the 5th-order schemes has 3 stages with the use of a 2nd-order GKS flux function. Another 5th-order scheme has 2 stages only, where a 3rd-order flux function is used. To further improve the efficiency of the 5th-order 2 stages GKS, a simplified 3rd-order GKS flux function is adopted [55]. Meanwhile, in order to present a complete high order gas kinetic schemes, the 3rd-order 1 stage multi-dimensional GKS [29] and the 4th-order 2 stage GKS [35] will be summarized in this paper as well. Thus a family of high order GKS from 3rd-order up to 5th-order will be presented. For spatial reconstruction, the WENO technique has achieved great success, especially on structured mesh. Since we are focusing on the improvement of time accuracy for the schemes, the same 5th-order WENOZ reconstruction [4] based on characteristic variables will be used for all schemes, including the 5th-order Godunov method with RK technique.

This paper is organized as follows. Section 2 introduces the multi-stage time integrating techniques. Section 3 gives a brief review of GKS flux solvers and introduces the numerical algorithm for MSMD GKS. Section 4 presents the numerical results from different schemes and their comparison with other standard high order methods with exact Riemann solver in terms of accuracy, efficiency, and robustness. Finally we end up with concluding remarks.

2. Multi-stage multi-derivative methods

The conservation laws

$$\mathbf{w}_t + \nabla \cdot \mathbf{F}(\mathbf{w}) = 0, \mathbf{w}(0, \mathbf{x}) = \mathbf{w}_0(\mathbf{x}), \mathbf{x} \in \Omega \subseteq \mathbb{R}^d, \tag{1}$$

for conserved mass, momentum, and energy \mathbf{w} can be written as

$$\mathbf{w}_t = -\nabla \cdot \mathbf{F}(\mathbf{w}).$$

With the spatial discretization \mathbf{w}^h and appropriate evaluation $-\nabla \cdot \mathbf{F}(\mathbf{w})$, the original PDEs become a system of ordinary differential equation (ODE)

$$\mathbf{w}_t^h = L(\mathbf{w}^h), t = t_n. \tag{2}$$

The well established numerical scheme for ODE can be used to solve this initial value problem.

For a smooth function L , the solution $\mathbf{w}(\Delta t)$ around $(t = t_n = 0)$ becomes

$$\begin{aligned} \mathbf{w}(\Delta t) = & \mathbf{w}(0) + \Delta t \mathbf{w}^{(1)}(0) + \frac{\Delta t^2}{2} \mathbf{w}^{(2)}(0) + \frac{\Delta t^3}{6} \mathbf{w}^{(3)}(0) \\ & + \frac{\Delta t^4}{24} \mathbf{w}^{(4)}(0) + \frac{\Delta t^5}{120} \mathbf{w}^{(5)}(0) + \dots + \frac{\Delta t^n}{n!} \mathbf{w}^{(n)}(0) + \mathcal{O}(\Delta t^{n+1}), \end{aligned} \tag{3}$$

where $\mathbf{w}^{(n)}(t) (n = 1, 2, 3, \dots)$ refers to

$$\mathbf{w}^{(n)}(t) = \frac{d^n \mathbf{w}(t)}{dt^n} = \frac{d^{n-1} L(\mathbf{w}(t))}{dt^{n-1}}. \tag{4}$$

For simplicity of presentation, we define $L = L(\mathbf{w}(t))$ and $L^{(n)} = d^n L(t)/dt^n$. A n th-order time marching scheme can be constructed straightforwardly if the time derivatives of $L^{(n)}$ up to $(n - 1)$ th-order are provided. However, under most circumstances, we can easily evaluate low order derivatives, such as L for the approximate Riemann solver, $L^{(1)}$ for the generalized Riemann problem (GRP) and the 2nd-order GKS flux function, and $L^{(2)}$ for the 3rd-order GKS flux function. A continuous construction of higher order derivatives becomes prohibited, such as the extremely complicated 4th-order GKS flux function [28]. Another approach, similar to RK method, is to introduce the middle stages. The update at t^{n+1} becomes a linear combination of L and their derivatives in the multiple stages. If L is used only, the traditional RK method is recovered. But, with the inclusion of $L^{(n)}$, the multi-stage multi-derivative (MSMD) method can be constructed.

2.1. Multi-stage multi-derivative high order method

Definition 1. According to [40], given a collection of real numbers $a_{ij}^{(1)}, a_{ij}^{(2)}, a_{ij}^{(3)}, b_i^{(1)}, b_i^{(2)}, b_i^{(3)}$, a multi-derivative (up to 3), s -stage method can be defined as the following

$$\mathbf{w}_{n+1} = \mathbf{w}_n + \Delta t \sum_{i=1}^s b_i^{(1)} L(\mathbf{w}^i) + \Delta t^2 \sum_{i=1}^s b_i^{(2)} L^{(1)}(\mathbf{w}^i) + \Delta t^3 \sum_{i=1}^s b_i^{(3)} L^{(2)}(\mathbf{w}^i), \tag{5}$$

Table 1
Butcher tableau for a multi-derivative (up to 3) multi-stage method.

c_1	$a_{11}^{(1)}$	\dots	$a_{1s}^{(1)}$	$a_{11}^{(2)}$	\dots	$a_{1s}^{(2)}$	$a_{11}^{(3)}$	\dots	$a_{1s}^{(3)}$
\vdots	\vdots	\ddots	\vdots	\vdots	\ddots	\vdots	\vdots	\ddots	\vdots
c_s	$a_{s1}^{(1)}$	\dots	$a_{ss}^{(1)}$	$a_{s1}^{(2)}$	\dots	$a_{ss}^{(2)}$	$a_{s1}^{(3)}$	\dots	$a_{ss}^{(3)}$
	$b_1^{(1)}$	\dots	$b_s^{(1)}$	$b_1^{(2)}$	\dots	$b_s^{(2)}$	$b_1^{(3)}$	\dots	$b_s^{(3)}$

Table 2
Butcher tableau for RK4.

0	0	0	0	0
1/2	1/2	0	0	0
1/2	0	1/2	0	0
1	0	0	1	0
	1/6	1/3	1/3	1/6

Table 3
Butcher tableau for RK5.

0	0	0	0	0	0	0
1/4	1/4	0	0	0	0	0
3/8	3/32	9/32	0	0	0	0
12/13	1932/2197	-7200/2197	7296/2197	0	0	0
1	439/216	-8	3680/513	-845/4104	0	0
1/2	-8/27	2	-3544/2565	1859/4104	-11/40	0
	16/135	0	6656/12825	28561/56430	-9/50	2/55

Table 4
Butcher tableau for one stage 3rd-order method (S103).

0	0	0	0
	1	1/2	1/6

where intermediate stage values are given by

$$\mathbf{w}^i = \mathbf{w}_n + \Delta t \sum_{j=1}^{i-1} a_{ij}^{(1)} L(\mathbf{w}^j) + \Delta t^2 \sum_{j=1}^{i-1} a_{ij}^{(2)} L^{(1)}(\mathbf{w}^j) + \Delta t^3 \sum_{j=1}^{i-1} a_{ij}^{(3)} L^{(2)}(\mathbf{w}^j). \tag{6}$$

Since MSMD is an explicit method, at every intermediate stage the state only depends on the states and derivatives of previous ones. The Butcher tableau, which is widely used to list all coefficients in Runge–Kutta and MSMD method [40], is shown in Table 1, where $c_i = \sum_{j=1}^s a_{ij}$. Note that the explicit method makes all coefficient $a_{ij} = 0$ if $i \leq j$.

In the following, a few cases which are related high order CFD methods are presented.

2.2. Traditional Runge–Kutta methods: RK4 and RK5

The Butcher tableau for classical 4th order, four-stages Runge–Kutta (RK4) [23] and 5th-order, six-stages Runge–Kutta (RK5) methods [12] are given in Table 2 and Table 3. The computational time and robustness of the above RK5 with Riemann solvers for the flux evaluation will be compared with our newly proposed 5th-order MSMD GKS methods. Since most high order schemes with Riemann solver use 3rd-order or 4th-order time accurate RK methods, in this paper the comparison will be done with 4th-order RK (RK4) scheme.

2.3. A 3rd-order 1 stage method: S103

A 3rd-order accurate GKS flux function provides up to 3rd-order time derivatives $\mathbf{w}^{(3)} = L^{(2)}$. A direct Taylor expansion method can be used to update the solution,

$$\mathbf{w}_{n+1} = \mathbf{w}_n + \Delta t L + \frac{1}{2} \Delta t^2 L^{(1)} + \frac{1}{6} \Delta t^3 L^{(2)}.$$

This is the 3rd-order one stage time-accuracy scheme [27,29,55]. The corresponding Butcher tableau is given in Table 4.

2.4. A 4th-order 2 stages method: S204

There is uniqueness for the 2 stages (S2) 4th-order (O4) method [5]. This method has been used in CFD applications [40,26,35], which show good accuracy, high efficiency, and robustness. It can be written as

Table 5
Butcher tableau for S204.

0	0	0	0	0
1/2	1/2	0	1/8	0
	1	0	1/6	1/3

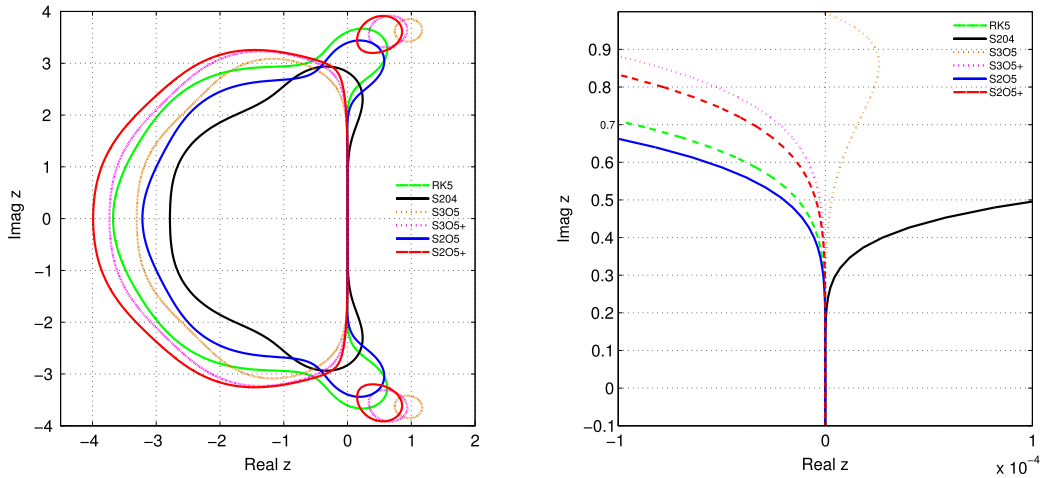


Fig. 1. Left figure: regions of absolute stability for RK5, S204, S205, S205+, S305, and S305+ schemes. Right figure: local enlarged region of left figure.

Table 6
Butcher tableau for S305.

0	0	0	0	0	0	0
2/5	2/5	0	0	2/25	0	0
1	1	0	0	-1/4	3/4	0
	1	0	0	1/8	25/72	1/36

$$\begin{aligned}
 \mathbf{w}^1 &= \mathbf{w}_n + \frac{1}{2} \Delta t L(\mathbf{w}_n) + \frac{1}{8} \Delta t^2 L^{(1)}(\mathbf{w}_n), \\
 \mathbf{w}_{n+1} &= \mathbf{w}_n + \Delta t L(\mathbf{w}_n) + \frac{1}{2} \Delta t^2 \left[\frac{1}{3} L^{(1)}(\mathbf{w}_n) + \frac{2}{3} L^{(1)}(\mathbf{w}^1) \right].
 \end{aligned}
 \tag{7}$$

The Butcher tableau for the two-stage fourth-order (S204) method is given in Table 5. The region of absolute stability is plotted in Fig. 1.

2.5. 5th-order 3 stage methods: S305

For the 5th-order MSMD methods, the coefficients are not uniquely defined. With the constraints of $a_{ij}^{(1)} = 0, j \neq 1$, several choices are given in [5]. The choices of the coefficients have been studied in [6]. However, the real performance from different schemes for the Euler and N-S equations haven't been reported yet. Here we will construct two kinds of 5th-order 3 stages (S305) methods. The first choice is given by:

$$\begin{aligned}
 \mathbf{w}^1 &= \mathbf{w}_n + \frac{2}{5} \Delta t L(\mathbf{w}_n) + \frac{2}{25} \Delta t^2 L^{(1)}(\mathbf{w}_n), \\
 \mathbf{w}^2 &= \mathbf{w}_n + \Delta t L(\mathbf{w}_n) + \frac{1}{2} \Delta t^2 \left[-\frac{1}{2} L^{(1)}(\mathbf{w}_n) + \frac{3}{2} L^{(1)}(\mathbf{w}^1) \right], \\
 \mathbf{w}_{n+1} &= \mathbf{w}_n + \Delta t L(\mathbf{w}_n) + \frac{1}{2} \Delta t^2 \left[\frac{1}{4} L^{(1)}(\mathbf{w}_n) + \frac{25}{36} L^{(1)}(\mathbf{w}^1) + \frac{1}{18} L^{(1)}(\mathbf{w}^2) \right],
 \end{aligned}
 \tag{8}$$

which is denoted by S305 and the Butcher tableau is given in Table 6. Note that $a_{31}^{(2)} = -1/4 < 0$.

Table 7
Butcher tableau for S305+.

0	0	0	0	0	0	0
3/10	3/10	0	0	9/200	0	0
3/4	3/4	0	0	0	9/32	0
	1	0	0	5/54	25/81	8/81

Table 8
Butcher tableau for S205.

0	0	0	0	0	0
2/5	2/5	0	2/25	0	0
1	1	0	1/2	0	1/16
					5/48

Table 9
Butcher tableau for S205+.

0	0	0	0	0	0
2/5	2/5	0	2/25	0	4/375
1	1	0	1/2	0	1/16
					5/48

The second choice is given by:

$$\begin{aligned}
 \mathbf{w}^1 &= \mathbf{w}_n + \frac{3}{10} \Delta t L(\mathbf{w}_n) + \frac{9}{200} \Delta t^2 L^{(1)}(\mathbf{w}_n), \\
 \mathbf{w}^2 &= \mathbf{w}_n + \frac{3}{4} \Delta t L(\mathbf{w}_n) + \frac{9}{32} \Delta t^2 L^{(1)}(\mathbf{w}^1), \\
 \mathbf{w}_{n+1} &= \mathbf{w}_n + \Delta t L(\mathbf{w}_n) + \frac{1}{2} \Delta t^2 \left[\frac{5}{27} L^{(1)}(\mathbf{w}_n) + \frac{50}{81} L^{(1)}(\mathbf{w}^1) + \frac{16}{81} L^{(1)}(\mathbf{w}^2) \right],
 \end{aligned}
 \tag{9}$$

which is named S305+ and the Butcher tableau is given in Table 7.

In comparison with S305, S305+ keeps all coefficients positive, which may have better stability property in numerical simulations. The numerical performance will be conducted in this paper, and S305+ does have a better robustness.

2.6. A 5th-order 2 stages methods: S205

To achieve fifth-order time accuracy, we may construct a scheme with 3rd-order derivatives and two stages [35]. The scheme is given by,

$$\begin{aligned}
 \mathbf{w}^1 &= \mathbf{w}_n + \frac{2}{5} \Delta t L(\mathbf{w}_n) + \frac{2}{25} \Delta t^2 L^{(1)}(\mathbf{w}_n), \\
 \mathbf{w}_{n+1} &= \mathbf{w}_n + \Delta t L(\mathbf{w}_n) + \frac{1}{2} \Delta t^2 L^{(1)}(\mathbf{w}_n) + \frac{1}{6} \Delta t^3 \left[\frac{3}{8} L^{(2)}(\mathbf{w}_n) + \frac{5}{8} L^{(2)}(\mathbf{w}^1) \right].
 \end{aligned}
 \tag{10}$$

The Butcher tableau for the 5th order two-stages (S205) scheme with up to 3rd-order derivatives is given in Table 8. The region of stability is plotted in Fig. 1.

For RK method, the range covered in the imaginary axis indicates the stability region. As shown in Fig. 1, the S204 method has the largest imaginary axis covered by the stability contour among all schemes. This is confirmed by the numerical results, which shows that S204 has best robustness. On the other hand, the S205 method in Table 8 shows the smallest region of absolute stability. However, for the S205 method the coefficient $a_{21}^{(3)}$ is a free parameter, which can be chosen to increase its stability without losing its accuracy. How to optimize this coefficient is still not clear. But, with the modified coefficients in Table 9, which is named S205+, the scheme improves the region of absolute stability, as shown in Fig. 1. The S205+ method contains the largest area of absolute stability on the negative left plane in Fig. 1. The improvement of robustness from S205+ will be shown in the numerical tests.

In the RK method, lot of efforts have been paid for minimizing the dissipation and dispersion error of the schemes [18], which is important in turbulence and acoustic computations. For different schemes in this paper, the dissipation rate and phase error defined in [18] are plotted in Fig. 2, where c is the wave speed for linear advection equation and k is the wave number. It shows that with the same time step both S305+ and S205+ have less dissipation and dispersion error than that of RK5. This indicates that high order MSMD methods have potential to present more accurate solutions than those with traditional RK technique.

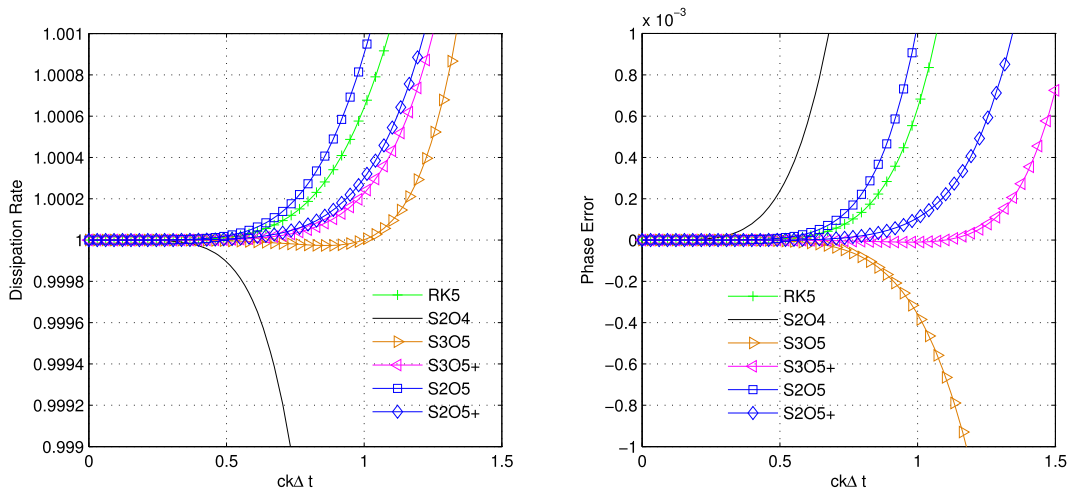


Fig. 2. The dissipation (Left) and dispersion (Right) properties for different schemes. Dissipation rate $||r| - 1| < 0.001$ and phase error $|\delta| < 0.001$ are set as accuracy limit in [18].

3. High order MSMD gas kinetic schemes

3.1. General finite volume framework and kinetic model equation

In a 2D rectangular mesh, Eq. (2) can be written in a semi-discrete form

$$\frac{d\bar{W}_{ij}^n}{dt} = L_{ij}(W) := -\frac{1}{\Delta x_{ij}}(F_{i+1/2,j}^n - F_{i-1/2,j}^n) - \frac{1}{\Delta y_{ij}}(G_{i,j+1/2}^n - G_{i,j-1/2}^n), \tag{11}$$

where $W = (\rho, \rho U, \rho V, \rho E)$ are the conservative flow variables, \bar{W} are the cell average values. Here $F(W(t)) = (F_\rho, F_{\rho U}, F_{\rho V}, F_{\rho E})$ are the corresponding fluxes across the cell interface in the x -direction, similarly for $G(W(t))$ in the y -direction. The key point for constructing MSMD method is to obtain a time dependent flux function $F(t)$ and $G(t)$. Most Godunov type schemes solve the Riemann problem with time-independent flux. But, for the GKS solver and generalized Riemann problem (GRP), time-dependent fluxes are provided.

The gas kinetic scheme is to solve the kinetic equation

$$f_t + \mathbf{u} \cdot \nabla f = \frac{g - f}{\tau}, \tag{12}$$

where \mathbf{u} is particle velocity. Here f is the gas distribution function, which is a function in the physical and velocity space, i.e., $f(x, y, t, u, v, \xi)$ as a function of particle velocity (u, v) , space and time coordinates (x, y, t) , and internal variable ξ . Here g is the corresponding equilibrium state of f , and τ is the relaxation time from f to g . The collision term satisfies the compatibility condition

$$\int \frac{g - f}{\tau} \psi d\Xi = 0, \tag{13}$$

where $\psi = (\psi_1, \psi_2, \psi_3, \psi_4)^T = (1, u, v, \frac{1}{2}(u^2 + v^2 + \xi^2))^T$, $d\Xi = dudvd\xi$, $d\xi = d\xi_1 d\xi_2 \dots d\xi_K$, K is the degrees of internal variable ξ with the relationship $K = (4 - 2\gamma)/(\gamma - 1)$ for a 2D problem, and γ is the specific heat ratio.

The connections between macroscopic mass ρ , momentum $(\rho U, \rho V)$, and energy ρE with the distribution function f are

$$\begin{pmatrix} \rho \\ \rho U \\ \rho V \\ \rho E \end{pmatrix} = \int \psi f d\Xi. \tag{14}$$

The time-dependent numerical fluxes across a cell interface, for example in the x -direction, can be evaluated by

$$F(t) = \int_{-\frac{1}{2}\Delta y}^{\frac{1}{2}\Delta y} \int u \psi f(0, y, t, u, v, \xi) d\Xi dy, \tag{15}$$

where the construction of the time-dependent cell interface distribution function f is the core of the gas kinetic scheme.

3.2. GKS flux solver

The integral solution of kinetic model equation is

$$f(0, y, t, u, v, \xi) = \frac{1}{\tau} \int_0^t g(-u(t-t'), y-v(t-t'), t', u, v, \xi) e^{-(t-t')/\tau} dt' + e^{-t/\tau} f_0(-ut, y-vt, u, v, \xi). \tag{16}$$

The initial term f_0 in the above integral solution is defined as,

$$f = f_0^l(x, y, u, v, \xi)H(x) + f_0^r(x, y, u, v, \xi)(1 - H(x)), \tag{17}$$

where $H(x)$ is the Heaviside function, f_0^l and f_0^r are the initial gas distribution functions on both sides of a cell interface. To keep a third-order accuracy, the gas distribution function in space around $(x, y) = (0, 0)$ can be expanded as

$$f_0^{l,r}(x, y) = f_0^{l,r}(0, 0) + \frac{\partial f_0^{l,r}}{\partial x}x + \frac{\partial f_0^{l,r}}{\partial y}y + \frac{1}{2} \frac{\partial^2 f_0^{l,r}}{\partial x^2}x^2 + \frac{\partial^2 f_0^{l,r}}{\partial x \partial y}xy + \frac{1}{2} \frac{\partial^2 f_0^{l,r}}{\partial y^2}y^2. \tag{18}$$

According to the Chapman–Enskog theory, for the Euler equations $f_0^{l,r}(0, 0)$ are the equilibrium states

$$f_0^{l,r}(0, 0) = g_0^{l,r}. \tag{19}$$

For the Navier–Stokes equations, they are given by

$$f_0^{l,r}(0, 0) = g_0^{l,r} - \tau \left(\frac{\partial g_0^{l,r}}{\partial x}u + \frac{\partial g_0^{l,r}}{\partial y}v + \frac{\partial g_0^{l,r}}{\partial t} \right), \tag{20}$$

where the Maxwellian distribution function $g_0^{l,r}$ are written as

$$g_0 = \rho \left(\frac{\lambda}{\pi} \right)^{\frac{K+2}{2}} e^{\lambda((u-U)^2 + (v-V)^2 + \xi^2)}, \tag{21}$$

where $\lambda = m/2kT$, and m, k, T represent the molecular mass, the Boltzmann constant, and temperature. $g_0^{l,r}$ are the equilibrium states corresponding to the macroscopic flow variables W_l, W_r at the left and right hand sides of a cell interface.

After determining the non-equilibrium part f_0 , the equilibrium part g in the integral solution can be expanded in space and time as follows

$$g = \bar{g} + \frac{\partial \bar{g}}{\partial x}x + \frac{\partial \bar{g}}{\partial y}y + \frac{\partial \bar{g}}{\partial t}t + \frac{1}{2} \frac{\partial^2 \bar{g}}{\partial x^2}x^2 + \frac{\partial^2 \bar{g}}{\partial x \partial y}xy + \frac{1}{2} \frac{\partial^2 \bar{g}}{\partial y^2}y^2 + \frac{1}{2} \frac{\partial^2 \bar{g}}{\partial t^2}t^2 + \frac{\partial^2 \bar{g}}{\partial x \partial t}xt + \frac{\partial^2 \bar{g}}{\partial y \partial t}yt, \tag{22}$$

where \bar{g} can be obtained using the compatibility condition in Eq. (13),

$$\int \psi \bar{g} d\Xi = \bar{W} = \int_{u>0} \psi g_l d\Xi + \int_{u<0} \psi g_r d\Xi. \tag{23}$$

Before calculating all derivatives, let's introduce the following notations

$$a_1 = g_x/g, a_2 = g_y/g, A = g_t/g, d_{11} = \frac{\partial a_1}{\partial x}, d_{12} = \frac{\partial a_1}{\partial y} = \frac{\partial a_2}{\partial x}, d_{22} = \frac{\partial a_2}{\partial y}, b_1 = \frac{\partial a_1}{\partial t} = \frac{\partial A}{\partial x}, b_2 = \frac{\partial a_2}{\partial t} = \frac{\partial A}{\partial y}, B = \frac{\partial A}{\partial t}. \tag{24}$$

All coefficients a_1, a_2, A, \dots are determined by conservative flow variables and their gradients. Each coefficient can be written as $\Lambda = \Lambda_1\psi_1 + \Lambda_2\psi_2 + \Lambda_3\psi_3 + \Lambda_4\psi_4$, which is determined in the following.

First order derivatives:

$$\langle a_1 \rangle = \frac{\partial W}{\partial x}, \langle a_2 \rangle = \frac{\partial W}{\partial y}, \langle A + a_1u + a_2v \rangle = 0. \tag{25}$$

Second order derivatives:

$$\begin{aligned} \langle a_1^2 + d_{11} \rangle &= \frac{\partial^2 W}{\partial x^2}, \langle a_2^2 + d_{22} \rangle = \frac{\partial^2 W}{\partial y^2}, \langle a_1 a_2 + d_{12} \rangle = \frac{\partial^2 W}{\partial x \partial y}, \\ \langle (a_1^2 + d_{11})u + (a_1 a_2 + d_{12})v + (A a_1 + b_1) \rangle &= 0, \\ \langle (a_1 a_2 + d_{12})u + (a_2^2 + d_{22})v + (A a_2 + b_2) \rangle &= 0, \\ \langle (A a_1 + b_1)u + (A a_2 + b_2)v + (A^2 + B) \rangle &= 0, \end{aligned} \tag{26}$$

where $\langle \dots \rangle$ are the moments of a gas distribution function defined by

$$\langle \dots \rangle = \int \psi g(\dots) d\Xi. \tag{27}$$

In the following subsections the final expressions for the 3rd-order and 2nd-order GKS flux functions are listed. The detailed consideration for the GKS flux construction is given in [47] for the 2nd-order flux and [29] for the 3rd-order one.

3.2.1. Full 3rd-order GKS flux in 2D

With the definition of a physical particle collision time τ and a numerical one τ_n for proving additional dissipation in unresolved region, the integral solution becomes

$$\begin{aligned} f(0, y, t, u, v, \xi) &= \frac{1}{\tau_n} \int_0^t g(-u(t-t'), y - v(t-t'), t', u, v, \xi) e^{-(t-t')/\tau_n} dt' \\ &+ e^{-t/\tau_n} f_0(-ut, y - vt, u, v, \xi). \end{aligned} \tag{28}$$

Substituting Eq. (18) and (22) with coefficients in Eq. (24) into the above equation, we get

$$\begin{aligned} &\frac{1}{\tau_n} \int_0^t g(-u(t-t'), y - v(t-t'), t', u, v, \xi) e^{-(t-t')/\tau_n} dt' \\ &= C_1 \bar{g} + C_2 \bar{g} \bar{a}_1 u + C_1 \bar{g} \bar{a}_2 y + C_2 \bar{g} \bar{a}_2 v + C_3 \bar{g} \bar{A} + \frac{1}{2} C_4 \bar{g} (\bar{a}_1^2 + \bar{d}_{11}) u^2 \\ &+ \frac{1}{2} C_1 \bar{g} (\bar{a}_2^2 + \bar{d}_{22}) y^2 + C_2 \bar{g} (\bar{a}_2^2 + \bar{d}_{22}) v y + \frac{1}{2} C_4 \bar{g} (\bar{a}_2^2 + \bar{d}_{22}) v^2 \\ &+ C_2 \bar{g} (\bar{a}_1 \bar{a}_2 + \bar{d}_{12}) u y + C_4 \bar{g} (\bar{a}_1 \bar{a}_2 + \bar{d}_{12}) u v + \frac{1}{2} C_5 \bar{g} (\bar{A}^2 + \bar{B}) \\ &+ C_6 \bar{g} (\bar{A} \bar{a}_1 + \bar{b}_1) u + C_3 \bar{g} (\bar{A} \bar{a}_2 + \bar{b}_2) y + C_6 \bar{g} (\bar{A} \bar{a}_2 + \bar{b}_2) v, \end{aligned} \tag{29}$$

and

$$e^{-t/\tau_n} f_0(-ut, y - vt, u, v, \xi) = \begin{cases} e^{-t/\tau_n} f_0^l(-ut, y - vt, u, v, \xi), & u > 0, \\ e^{-t/\tau_n} f_0^r(-ut, y - vt, u, v, \xi), & u < 0, \end{cases} \tag{30}$$

where

$$\begin{aligned} &e^{-t/\tau_n} f_0^{l,r}(-ut, y - vt, u, v, \xi) \\ &= C_7 g_0^{l,r} [1 - \tau (a_1^{l,r} u + a_2^{l,r} v + A^{l,r})] \\ &+ C_8 g_0^{l,r} [a_1^{l,r} u - \tau ((a_1^{l,r})^2 + d_{11}^{l,r}) u^2 + (a_1^{l,r} a_2^{l,r} + d_{12}^{l,r}) u v + (A^{l,r} a_1^{l,r} + b_1^{l,r}) u] \\ &+ C_7 g_0^{l,r} [a_2^{l,r} v - \tau ((a_1^{l,r} a_2^{l,r} + d_{12}^{l,r}) u + ((a_2^{l,r})^2 + d_{22}^{l,r}) v + A^{l,r} a_2^{l,r} + b_2^{l,r})] y \\ &+ C_8 g_0^{l,r} [a_2^{l,r} v - \tau ((a_1^{l,r} a_2^{l,r} + d_{12}^{l,r}) u v + ((a_2^{l,r})^2 + d_{22}^{l,r}) v^2 + (A^{l,r} a_2^{l,r} + b_2^{l,r}) v)] \\ &+ \frac{1}{2} C_9 g_0^{l,r} ((a_1^{l,r})^2 + d_{11}^{l,r}) u^2 + \frac{1}{2} C_7 g_0^{l,r} ((a_2^{l,r})^2 + d_{22}^{l,r}) y^2 \\ &+ C_8 g_0^{l,r} ((a_2^{l,r})^2 + d_{22}^{l,r}) v y + \frac{1}{2} C_9 g_0^{l,r} ((a_2^{l,r})^2 + d_{22}^{l,r}) v^2 \\ &+ C_8 g_0^{l,r} (a_1^{l,r} a_2^{l,r} + d_{12}^{l,r}) u y + C_9 g_0^{l,r} (a_1^{l,r} a_2^{l,r} + d_{12}^{l,r}) u v. \end{aligned} \tag{31}$$

The time integral coefficients are given by

$$\begin{aligned} C_1 &= 1 - e^{-t/\tau_n}, C_2 = (t + \tau)e^{-t/\tau_n} - \tau, C_3 = t - \tau + \tau e^{-t/\tau_n}, C_4 = (-t^2 - 2\tau t)e^{-t/\tau_n}, \\ C_5 &= t^2 - 2\tau t, C_6 = -\tau t(1 + e^{-t/\tau_n}), C_7 = e^{-t/\tau_n}, C_8 = -te^{-t/\tau_n}, C_9 = t^2 e^{-t/\tau_n}. \end{aligned} \tag{32}$$

3.2.2. Simplified 3rd-order GKS flux in 2D

The full 3rd-order flux function is very complicated. A simplified version has been proposed by Zhou et al. [55]. The new set of coefficients is introduced as

$$\begin{aligned} a_x &= a_1 = g_x/g, a_y = a_2 = g_y/g, a_t = A = g_t/g, \\ a_{xx} &= g_{xx}/g, a_{xy} = g_{xy}/g, a_{yy} = g_{yy}/g, \\ a_{xt} &= g_{xt}/g, a_{yt} = g_{yt}/g, a_{tt} = g_{tt}/g. \end{aligned} \tag{33}$$

And Eq. (25) and (26) are replaced by

$$\begin{aligned} \langle a_x \rangle &= \frac{\partial W}{\partial x}, \langle a_y \rangle = \frac{\partial W}{\partial y}, \langle a_t + a_x u + a_y v \rangle = 0, \\ \langle a_{xx} \rangle &= \frac{\partial^2 W}{\partial x^2}, \langle a_{xy} \rangle = \frac{\partial^2 W}{\partial x \partial y}, \langle a_{yy} \rangle = \frac{\partial^2 W}{\partial y^2}, \\ \langle a_{xx} u + a_{xy} v + a_{xt} \rangle &= 0, \\ \langle a_{xy} u + a_{yy} v + a_{yt} \rangle &= 0, \\ \langle a_{xt} u + a_{yt} v + a_{tt} \rangle &= 0. \end{aligned} \tag{34}$$

The final distribution function becomes

$$\begin{aligned} f(0, y, t, u, v, \xi) &= \bar{g} + \frac{1}{2} \bar{g}_{yy} y^2 + \bar{g}_t t + \frac{1}{2} \bar{g}_{tt} t^2 - \tau [(\bar{g}_t + u \bar{g}_x + v \bar{g}_y) + (\bar{g}_{tt} + u \bar{g}_{xt} + v \bar{g}_{yt}) t] \\ &\quad - e^{-t/\tau_n} [\bar{g} - (u \bar{g}_x + v \bar{g}_y) t] \\ &\quad + e^{-t/\tau_n} [g^l - (u g_x^l + v g_y^l) t] H(u) + e^{-t/\tau_n} [g^r - (u g_x^r + v g_y^r) t] (1 - H(u)). \end{aligned} \tag{35}$$

Both the full and simplified 3rd-order GKS fluxes could achieve the theoretical accuracies. The reason may come from the insensitivity of macroscopic flux function to the microscopic particle distribution function once the conservation is fully imposed in the evolution process. Since the simplified 3rd-order flux has about 4 times speed-up in comparison with the complete 3rd-order one in the 2D case, the simplified flux function will be used in all test cases in this paper.

3.2.3. 2nd-order GKS flux in 2D

If we drop all second-order derivative in Eq. (29) and Eq. (31), the traditional 2nd-order GKS flux solver can be recovered

$$\begin{aligned} f(0, y, t, u, v, \xi) &= (1 - e^{-t/\tau_n}) \bar{g} + ((t - \tau)e^{-t/\tau_n} - \tau)(u \bar{a}_1 + v \bar{a}_2) + (t - \tau + \tau e^{-t/\tau_n}) \bar{A} g_0 \\ &\quad + e^{-t/\tau_n} [g^l - (u g_x^l + v g_y^l)(\tau + t) - \tau A_r] H(u) \\ &\quad + e^{-t/\tau_n} [g^r - (u g_x^r + v g_y^r)(\tau + t) - \tau A_l] (1 - H(u)). \end{aligned} \tag{36}$$

3.3. Numerical algorithm for MSMD GKS

The numerical flux of the GKS is a complicated function of time in the non-smooth region. In order to construct MSMD GKS, the 1st-order and 2nd-order time derivatives of the flux function have to be properly evaluated. Since the main contribution of a flux function in a numerical scheme is about the total transport within a time step between cells, the time derivatives of a flux function are evaluated on the average of a time step. Denote the total transport of flux at the cell interface $i + 1/2$ within a time interval δ ,

$$\mathbb{F}_{i+1/2}(W^n, \delta) = \int_{t_n}^{t_n+\delta} F_{i+1/2}(W^n, t) dt = \int_{t_n}^{t_n+\delta} \int u \psi f(x_{i+1/2}, t, u, v, \xi) d\Xi dt.$$

For a 2nd-order GKS flux, the flux can be approximated to be a linear function within a time step,

$$F_{i+1/2}(W^n, t) = F_{i+1/2}^n + \partial_t F_{i+1/2}^n t. \tag{37}$$

The coefficients $F_{j+1/2}^n$ and $\partial_t F_{j+1/2}^n$ can be determined as follows

$$\begin{aligned} F_{i+1/2}^n \Delta t + \frac{1}{2} \partial_t F_{i+1/2}^n \Delta t^2 &= \mathbb{F}_{i+1/2}(W^n, \Delta t) \\ \frac{1}{2} F_{i+1/2}^n \Delta t + \frac{1}{8} \partial_t F_{i+1/2}^n \Delta t^2 &= \mathbb{F}_{i+1/2}(W^n, \Delta t/2) \end{aligned}$$

By solving the linear system, we have

$$\begin{aligned} F_{i+1/2}^n &= (4\mathbb{F}_{i+1/2}(W^n, \Delta t/2) - \mathbb{F}_{i+1/2}(W^n, \Delta t)) / \Delta t, \\ \partial_t F_{i+1/2}^n &= 4(\mathbb{F}_{i+1/2}(W^n, \Delta t) - 2\mathbb{F}_{i+1/2}(W^n, \Delta t/2)) / \Delta t^2. \end{aligned} \tag{38}$$

Similar formulation can be obtained for the flux in the y -direction.

For the 3rd-order GKS flux, $F(t)$ is approximated by a quadratic function of time with second-order time derivative,

$$F_{i+1/2}(W^n, t) = F_{i+1/2}^n + \partial_t F_{i+1/2}^n t + \frac{1}{2} \partial_{tt} F_{i+1/2}^n t^2. \tag{39}$$

Three conditions

$$\begin{aligned} F_{i+1/2}^n \Delta t + \frac{1}{2} \partial_t F_{i+1/2}^n \Delta t^2 + \frac{1}{6} \partial_{tt} F_{i+1/2}^n \Delta t^3 &= \mathbb{F}_{i+1/2}(W^n, \Delta t), \\ \frac{2}{3} F_{i+1/2}^n \Delta t + \frac{2}{9} \partial_t F_{i+1/2}^n \Delta t^2 + \frac{4}{81} \partial_{tt} F_{i+1/2}^n \Delta t^3 &= \mathbb{F}_{i+1/2}(W^n, 2\Delta t/3), \\ \frac{1}{3} F_{i+1/2}^n \Delta t + \frac{1}{18} \partial_t F_{i+1/2}^n \Delta t^2 + \frac{1}{162} \partial_{tt} F_{i+1/2}^n \Delta t^3 &= \mathbb{F}_{i+1/2}(W^n, \Delta t/3) \end{aligned}$$

can be used to determine these coefficients

$$\begin{aligned} F_{i+1/2}^n &= \frac{1}{\Delta t} (\mathbb{F}_{i+1/2}(W^n, \Delta t) - \frac{9}{2} \mathbb{F}_{i+1/2}(W^n, 2\Delta t/3) + 9\mathbb{F}_{i+1/2}(W^n, \Delta t/3)), \\ \partial_t F_{i+1/2}^n &= -\frac{9}{\Delta t^2} (\mathbb{F}_{i+1/2}(W^n, \Delta t) - 4\mathbb{F}_{i+1/2}(W^n, 2\Delta t/3) + 5\mathbb{F}_{i+1/2}(W^n, \Delta t/3)), \\ \partial_{tt} F_{i+1/2}^n &= \frac{9}{\Delta t^3} (3\mathbb{F}_{i+1/2}(W^n, \Delta t) - 9\mathbb{F}_{i+1/2}(W^n, 2\Delta t/3) + 9\mathbb{F}_{i+1/2}(W^n, \Delta t/3)). \end{aligned} \tag{40}$$

3.4. Remarks on spatial reconstructions

In 1-D case, the standard WENO5-Z reconstruction [4] based on characteristic variables is applied to obtain the cell interface values $W^{l,r}$.

In 2-D case, the reconstruction is conducted direction by direction, and the multi dimensional effect is included through the flux evaluation at Gaussian quadrature points on each cell interface. For example, at the cell interface $(i + 1/2, j)$, 1-D WENO5-Z reconstruction is first applied to get interface averaged values $\tilde{W}_{i+1/2,j}^{l,r}$ by using the averaged values within the neighboring cells $W_{i-2,j} \dots W_{i+3,j}$. Then, the tangential reconstruction based on $\tilde{W}_{i+1/2,j-2}^{l,r} \dots \tilde{W}_{i+1/2,j+2}^{l,r}$ is conducted by using the 1-D WENO5-Z again in the y -direction to obtain the values at the Gaussian points. The flux transport in the x -direction through the three Gaussian points is evaluated by quadratures

$$\frac{1}{\Delta y} \int_{y_{j-1/2}}^{y_{j+1/2}} F(W(x_{i+1/2}, y, t)) dy = \sum_{l=1}^3 \omega_l F(W(x_{i+1/2}, y_l, t)), \tag{41}$$

where $y_l = 0, \pm \frac{1}{2} \sqrt{\frac{3}{5}} \Delta y$ and $\omega_l = \frac{4}{9}, \frac{5}{18}, \frac{5}{18}$ accordingly. This guarantees a fifth-order accuracy for the flux calculation in the tangential direction. This reconstruction procedure is exactly the same as the Class B method defined in [53].

For GKS, besides the point-wise values at a cell interface, the slopes on both sides of a cell interface are also needed in the flux evaluations. For the initial discontinuous non-equilibrium part $g_0^{l,r}|_{x_{i+1/2}, y_l}$, they have one to one correspondences to $W_{i+1/2,j_l}^{l,r}$ at each Gaussian point, which are reconstructed in the same way as that for the Riemann solvers. For the equilibrium part \bar{g} , the interface averaged value $\tilde{W}_{i+1/2,j}$ is obtained by Eq. (23). Since \bar{g} represents a continuous equilibrium flow, a 4th-order polynomial can be uniquely determined by using $\tilde{W}_{i+1/2,j-2} \dots \tilde{W}_{i+1/2,j+2}$ and the point-wise value $\tilde{W}_{i+1/2,j_l}$ can be obtained.

For the non-equilibrium state within each cell i , based on the reconstructed cell interface values $(W_{i-1/2}^r, W_{i+1/2}^l)$ and cell averaged W_i , a 2nd order polynomial could be constructed within the cell. For the equilibrium state reconstruction at

the cell interface $i + 1/2$, the stencil is the four cell average values $W_{i-1} \dots W_{i+2}$ and the interface value $\bar{W}_{i+1/2}$ itself. Then, a 4th-order polynomial could be obtained without using any limiter. This equilibrium construction has a 5th-order accuracy in smooth region. The detail construction could be found in [29].

In the 2-D case, at the cell interface $(i + 1/2, j)$, after obtaining the interface averaged derivatives $\partial_x \bar{W}^{l,r}$, $\partial_{xx} \bar{W}^{l,r}$, the derivatives at each Gaussian point is constructed by the same WENO reconstruction in tangential direction as for the reconstruction of $W^{l,r}$. On the other hand, after obtaining $W^{l,r}$ at these three Gaussian points, $\partial_y W^{l,r}$, $\partial_{yy} W^{l,r}$ could be determined by a 2nd-order polynomial which passes through these three points. And $\partial_{xy} W^{l,r}$ could be calculated in the same way from the data $\partial_x W^{l,r}$ at the Gaussian points. For the equilibrium part, rather than the WENO reconstruction, a 4th-order polynomial is used to determine all derivatives along the tangential direction, and a 5th-order accuracy can be achieved in smooth region.

Since the Gaussian points are used to evaluate the flux transport along the cell interface, the y and y^2 terms in Eq. (29), (31), and (35) can be ignored in the flux evaluation.

4. Numerical tests

The schemes tested in this section include many MSMD GKS methods. The names of the schemes are defined as SnOr with the definition of n -stages and r th-order accuracy, such as S1O2 (single stage, 2nd-order accuracy), S1O3 (single stage, 3rd-order accuracy), etc. Here S3O5 (three stages, 5th-order) takes the time marching strategy in Table 6, while S3O5+ takes the strategy in Table 7. For different kinds of S2O5 schemes, the suffix “c” and “s” indicates its usage of complete 3rd-order flux or the simplified one. And the suffix “+” refers the coefficients in Table 9, while the absence of “+” refers the one in Table 8. If no special illustration, the numerical results in comparison, especially with the Godunov type schemes, are based on the same spatial reconstruction.

For inviscid flow computations, the physical collision time $\tau = \mu/p = 0$, where μ is the dynamical viscosity coefficient and p is the pressure, the numerical collision time

$$\tau_n = C_1 \Delta t + C_2 \left| \frac{p_l - p_r}{p_l + p_r} \right| \Delta t,$$

where C_1, C_2 are two constants. Generally, $C_1 \ll 1$ and $C_2 \sim \mathcal{O}(1)$ under current WENOZ reconstruction. For viscous flow computation, the physical collision time is defined as $\tau = \mu/p$ and the numerical collision time is

$$\tau_n = \frac{\mu}{p} + C_2 \left| \frac{p_l - p_r}{p_l + p_r} \right| \Delta t.$$

4.1. Accuracy tests

For the Euler equations, the smooth density propagation is used for the accuracy evaluation. In these cases, both the physical viscosity and the collision time related to the numerical dissipation are set to zero. The initial condition for the 1-D density advection is given by

$$\rho(x) = 1 + 0.2 \sin(\pi x), U(x) = 1, p(x) = 1, x \in [0, 2].$$

The exact solution under periodic boundary condition is

$$\rho(x, t) = 1 + 0.2 \sin(\pi(x - t)), U(x, t) = 1, p(x, t) = 1.$$

The numerical solutions from different schemes after one period of propagation at time $t = 2$ are obtained and compared with the exact solution. Since the same fifth-order spatial reconstruction is used for all schemes, the leading truncation error of a r th-order GKS is expected to be $\mathcal{O}(\Delta x^5 + \Delta t^r)$. Assume that $\Delta t = c \Delta x$ with the CFL condition, the truncation error is then proportional to $\mathcal{O}(\Delta x^5 + c^r (\Delta x)^r)$. If $c \ll 1$, the leading error of $\mathcal{O}(\Delta x^5)$ due to spatial discretization might become dominant, and it is hard to evaluate the time accuracy. So a rather large time step $\Delta t = 0.25 \Delta x$, which corresponds to $CFL \approx 0.5$, is used to test the spatial and temporal accuracy together. Based on L^1 error, the orders of different schemes at $t = 2$ are presented in Table 10.

All schemes from 2nd-order up to 5th-order ones achieve their theoretical accuracy. Among all schemes, the 5th-order 2-stages method with the complete 3rd-order GKS flux function has the smallest absolute error, while the same scheme with simplified 3rd-order GKS flux function has slightly larger absolute error. But, the order of accuracy of the scheme with simplified flux keeps the theoretical value.

The test is extended to 2-D case, where the density perturbation propagates in the diagonal direction,

$$\begin{aligned} \rho(x, y) &= 1 + 0.2 \sin(\pi x) \sin(\pi y), \\ U(x, y) &= 1, V(x, y) = 1, p(x) = 1, \end{aligned}$$

Table 10

Accuracy test for the 1-D advection of density perturbation by GKS with different temporal accuracy under same fifth order reconstruction. $\Delta t = 0.25\Delta x$.

Mesh	S1O2		S1O3		S2O4	
	L^1 error	Order	L^1 error	Order	L^1 error	Order
160	1.6449e-005		6.465536e-008		1.762567e-009	
320	4.11231e-006	2.000	7.934459e-009	3.027	5.558891e-011	4.954
640	1.02808e-006	2.000	9.871997e-010	3.001	1.793678e-012	5.166
1280	2.57021e-007	2.000	1.232565e-010	3.001	6.391980e-014	4.811
Mesh	S3O5		S3O5+		S2O5c	
	L^1 error	Order	L^1 error	Order	L^1 error	Order
160	1.72333e-09		1.72327e-09		1.55396e-09	
320	5.38507e-11	5.000	5.38492e-11	5.000	4.85575e-11	5.000
640	1.68291e-12	5.000	1.68297e-12	5.000	1.51832e-12	5.000
1280	5.36963e-14	4.970	5.34834e-14	4.976	4.82038e-14	4.977
Mesh	S2O5c+		S2O5s		S2O5s+	
	L^1 error	Order	L^1 error	Order	L^1 error	Order
160	1.55413e-09		1.55396e-09		1.578850e-009	
320	4.85622e-11	5.000	4.85568e-11	5.000	4.933414e-011	5.000
640	1.51805e-12	5.000	1.51805e-12	5.000	1.541736e-012	5.000
1280	4.83028e-14	4.974	4.90587e-14	4.952	4.924277e-014	4.969

Table 11

Accuracy test for the 2D advection of density perturbation for S3O5+ scheme, $\Delta t = 0.1\Delta x$.

Mesh	L^1 error	Order	L^2 error	Order	L^∞ error	Order
20*20	3.67810e-06		4.46724e-06		8.88218e-06	
40*40	5.85160e-08	5.974	7.09236e-08	5.976	1.40828e-07	5.979
80*80	9.17888e-10	5.994	1.11208e-09	5.995	2.20522e-09	5.997
160*160	1.43537e-11	5.999	1.73878e-11	5.999	3.44513e-11	6.000
320*320	2.24360e-13	5.999	2.71745e-13	6.000	5.435787e-13	5.989

Table 12

Accuracy test for the 2D advection of density perturbation for S2O5s+ scheme, $\Delta t = 0.1\Delta x$.

Mesh	L^1 error	Order	L^2 error	Order	L^∞ error	Order
20*20	3.63607e-06		4.41462e-06		8.77532e-06	
40*40	5.78414e-08	5.974	7.00846e-08	5.976	1.39129e-07	5.979
80*80	9.07345e-10	5.994	1.09893e-09	5.995	2.17865e-09	5.997
160*160	1.41889e-11	5.999	1.71825e-11	5.999	3.40366e-11	6.000
320*320	2.21805e-13	5.999	2.68546e-13	6.000	5.38458e-13	5.981

with the exact solution

$$\rho(x, y) = 1 + 0.2 \sin(\pi(x - t)) \sin(\pi(y - t)),$$

$$U(x, y) = 1, V(x, y) = 1, p(x) = 1.$$

The computation domain is $[-1, 1] \times [-1, 1]$ and the $N \times N$ uniform mesh points are used with periodic boundary condition. The results are shown in Table 11 and 12, with validated theoretical accuracy.

4.2. One dimensional test cases

Three Riemann problems in 1-D are selected to validate the high order GKS. At the same time, the results from the RK4 Godunov method with exact Riemann solver are also included. All simulations are based on the same initial reconstruction.

(a) Sod problem

The initial condition for the Sod problem is given by

$$(\rho, u, p) = \begin{cases} (1, 0, 1), & 0 < x < 0.5, \\ (0.125, 0, 0.1), & 0.5 \leq x < 1. \end{cases}$$

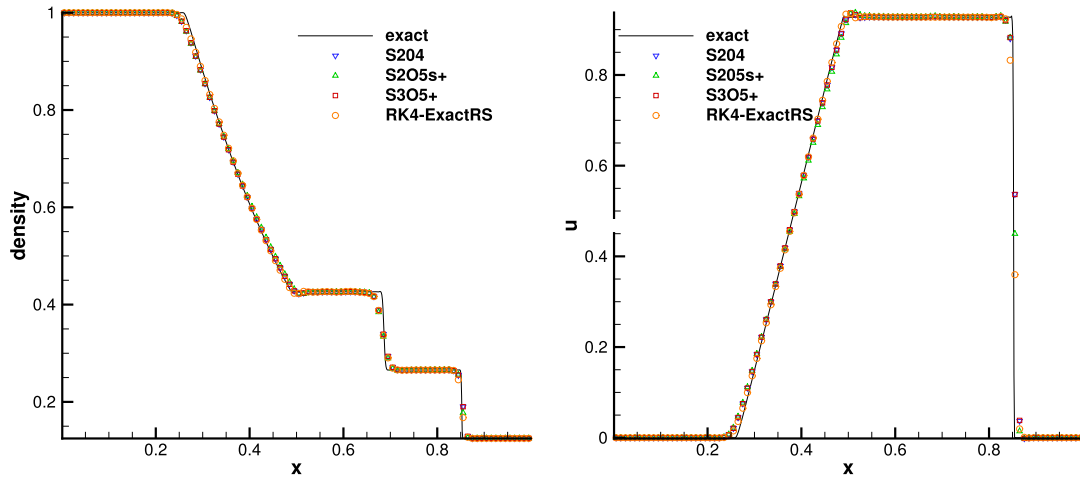


Fig. 3. The density and velocity distributions for 1-D sod problem at $t = 0.2$ with 100 cells.

The simulation domain is covered by 100 uniform mesh points. The solutions at $t = 0.2$ are presented. The WENO5-Z reconstruction is used on the characteristic variables. The results from S204, S205s+, S305+, and the exact Riemann solver are shown in Fig. 3.

(b) Blast wave problem

The initial conditions for the blast wave problem are given as follows

$$(\rho, u, p) = \begin{cases} (1, 0, 1000), & 0 \leq x < 10, \\ (1, 0, 0.01), & 0.1 \leq x < 90, \\ (1, 0, 100), & 0.9 \leq x \leq 100. \end{cases}$$

The computational domain is covered with 400 uniform mesh points and reflection boundary conditions are applied at both ends. The CFL number takes 0.5. The density and velocity distributions at $t = 3.8$ are presented in Fig. 4. All schemes give almost identical results. Based on the above observations, it seems that the Sod and blast wave cases may not be the appropriate tests to distinguish different kinds of high order schemes.

(c) Titarev and Toro problem

Titarev and Toro [43] problem is about high frequency oscillating sinusoidal waves propagation with shock interaction, which is a great challenge for spatial reconstruction [1,31] and flux solver [43]. The initial conditions are given as follows

$$(\rho, u, p) = \begin{cases} (1.515695, 0.523346, 1.805), & 0 \leq x < 0.5, \\ (1 + 0.1 \sin(20\pi x), 0, 1), & 0.5 \leq x < 10. \end{cases}$$

A uniform mesh with 1000 mesh points are used in the computational domain and $CFL = 0.5$ is used for all schemes. The result at $t = 5$ is shown in Fig. 5. Different from previous test cases, there are clear differences among GKS and Riemann solutions in the middle region, after shock interaction with smooth acoustic wave. All multi-stage schemes present less dissipative results than those from the high order RK4 Godunov method with exact Riemann solver. With the same initial reconstruction, the differences must come from the different type of temporal discretization and flux functions. This test case indicates the usefulness of the high order GKS on acoustic wave computations.

4.3. Two dimensional inviscid test cases

(a) Isentropic vortex propagation with 100 periods

The isentropic vortex propagation is tested in a 2-D domain for the smooth inviscid flow. The initial condition is given by

$$\begin{aligned} (U, V) &= (1, 1) + \frac{\kappa}{2\pi} e^{0.5(1-r^2)} (-\bar{y}, \bar{x}), \\ T &= 1 - \frac{(\gamma - 1)\kappa^2}{8\gamma\pi^2} e^{1-\gamma^2}, \\ S &= 1, \end{aligned} \tag{42}$$

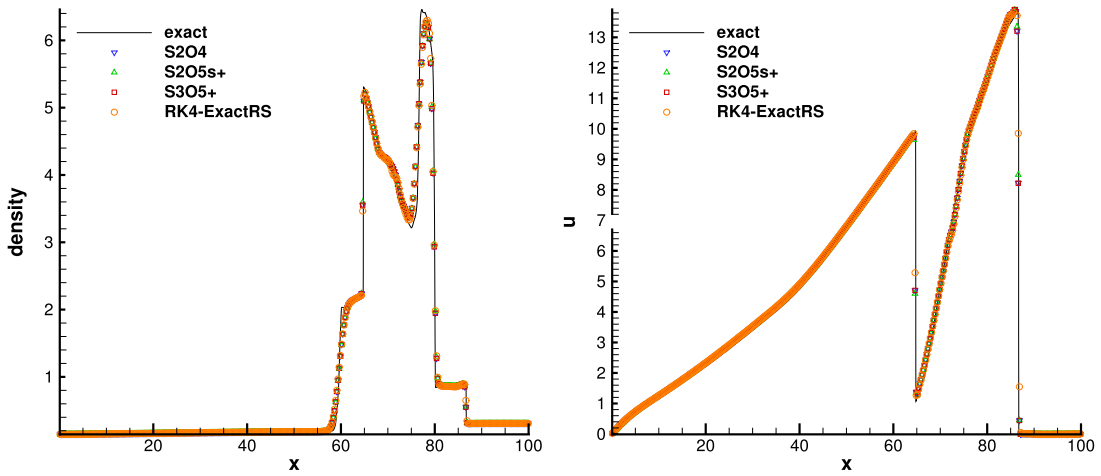


Fig. 4. The density and velocity distributions for 1-D blast wave problem at $t = 3.8$ with 400 cells.

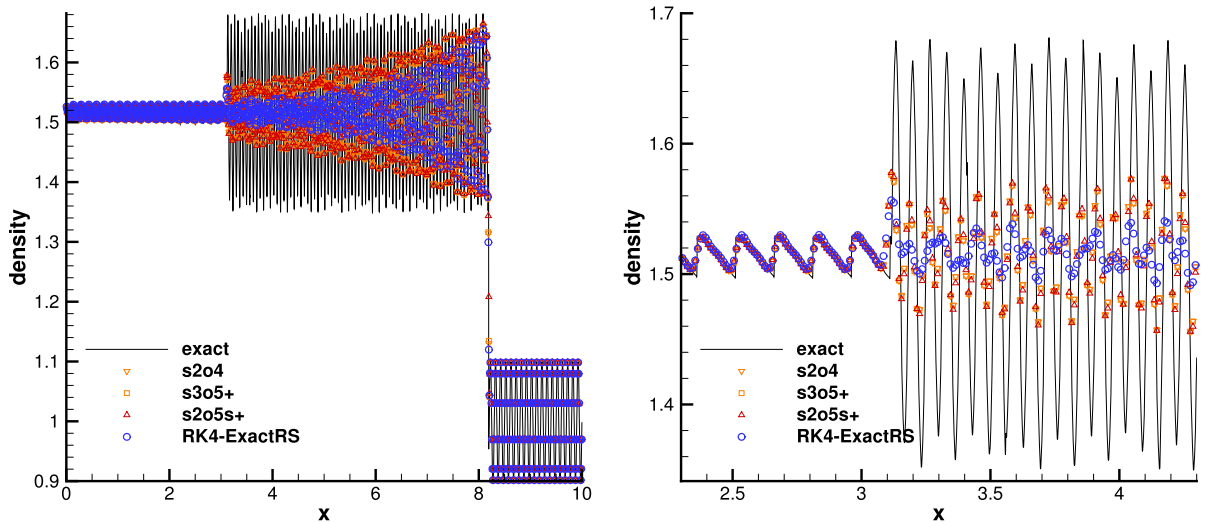


Fig. 5. The density distributions for 1-D Titarev–Toro problem at $t = 5.0$ with 1000 cells. Left figure: solution in the whole domain. Right figure: local enlargement.

where the density ρ and pressure p are calculated from the temperature T and the entropy S by

$$T = \frac{p}{\rho}, S = \frac{p}{\rho^\gamma}, \tag{43}$$

where $(\bar{x}, \bar{y}) = (x - 5, y - 5)$, $r^2 = \bar{x}^2 + \bar{y}^2$, and the vortex strength $\kappa = 5$. The computational domain is $[0, 10] \times [0, 10]$. Periodic boundary condition is applied to all boundaries.

To show performance of different time marching schemes, this case is tested under 1 period, 10 periods, and 100 periods, with $t = 10, 100$, and 1000 accordingly. Again, the same spatial reconstruction is used for all schemes. For $t = 10$ and $t = 100$, the error in density is less than 10^{-4} for all schemes, which could hardly be used to distinguish the performance of different high order schemes. However, with the output time $t = 1000$ for 100 periods vortex propagation, the one step 3rd-order S1O3c scheme shows the dispersion and dissipation error, see in Fig. 6, while other higher order schemes still keep the vortex center in the computational domain. It shows that the higher order time accurate scheme is important for capturing long time wave propagating behavior. Another observation is the anti-diffusive effect in the S1O3 and RK5 Godunov method with exact Riemann solver. A more quantitative comparison of the density distributions along $y = 0.0$ are shown in Fig. 7. It demonstrates that the close coupling of space and time evolution is important for capturing long time wave propagation.

(b) Two dimensional Riemann problems

For high speed compressible flow, two distinguishable flow patterns are the shock–vortex interaction and free shear layer [13]. Here, two dimensional Riemann problems are used for the study the complicated wave structures [25]. Although

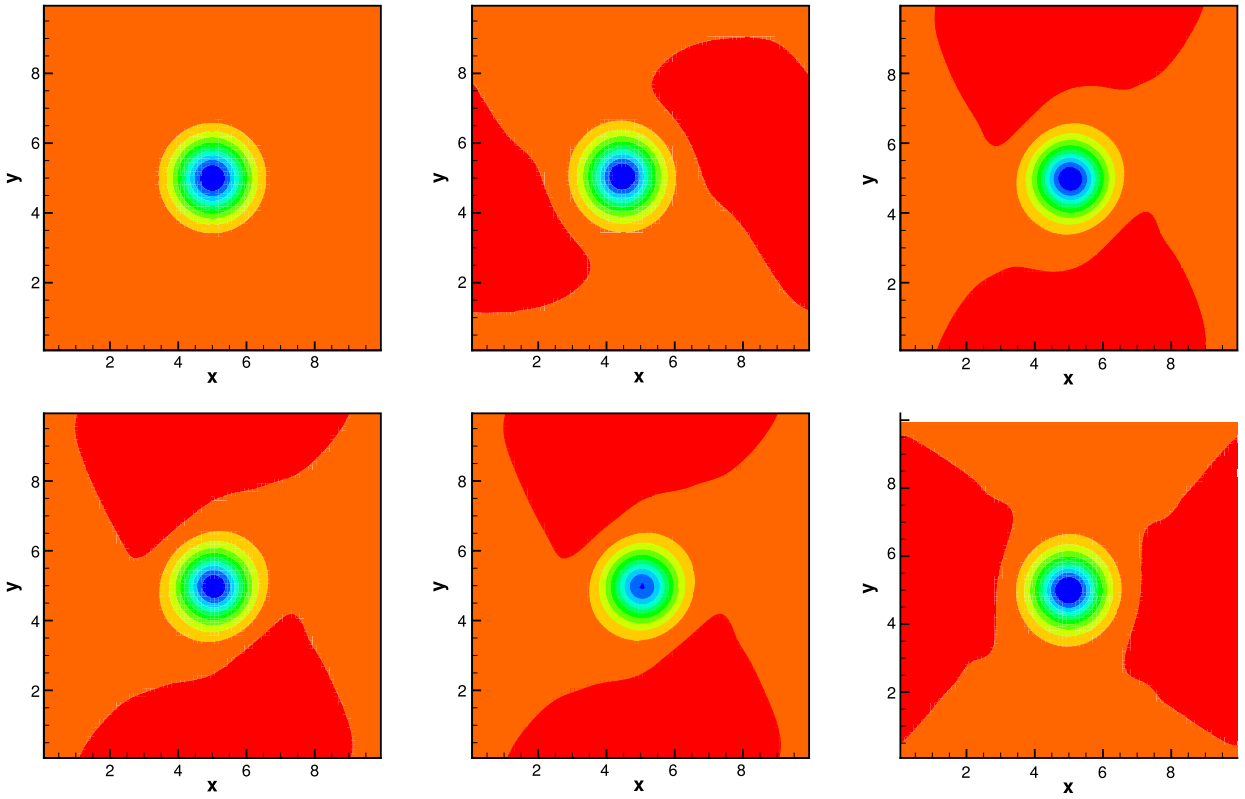


Fig. 6. The density contours of isentropic vortex propagation after 100 periods. CFL = 0.4, mesh 80×80 . Up row from left to right: exact solution, S103c, and S204. Down row from left to right: S205s+, S305+, RK5-ExactRS.

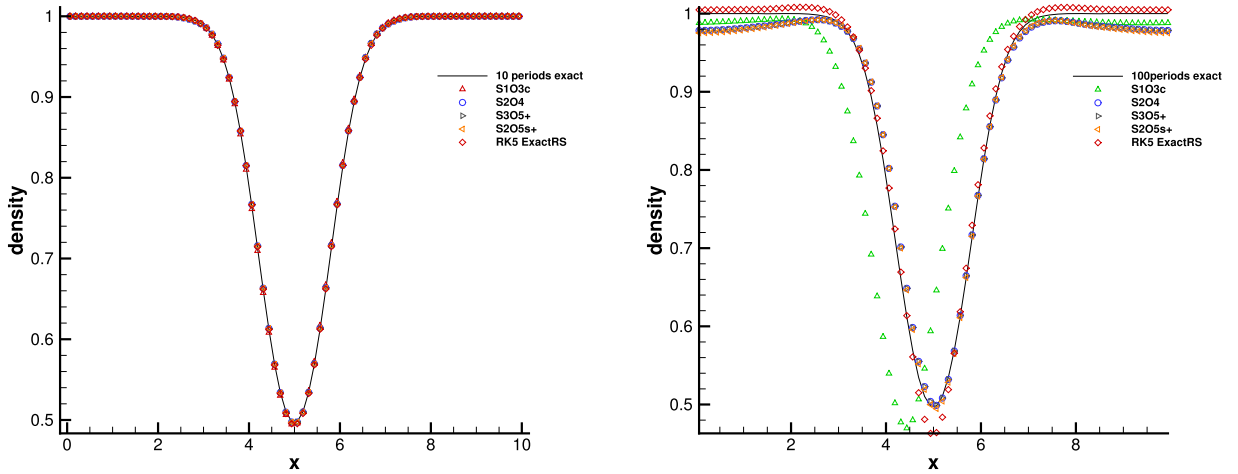


Fig. 7. Density distributions for isentropic vortex propagation along $y = 0$. Left: 10 periods. Right: 100 periods. 80×80 mesh points are used in the above calculations.

both test cases are for the inviscid flow, the inherent numerical viscosity in schemes can trigger shear instability. Another advantage for using 2-D Riemann problem is the rectangular domain and simple boundary condition.

(b1) Interaction of planar shocks

Configuration 3 in [25] involves the shock–shock interaction and shock–vortex interaction. The initial condition in a square domain $[0, 1] \times [0, 1]$ is given by

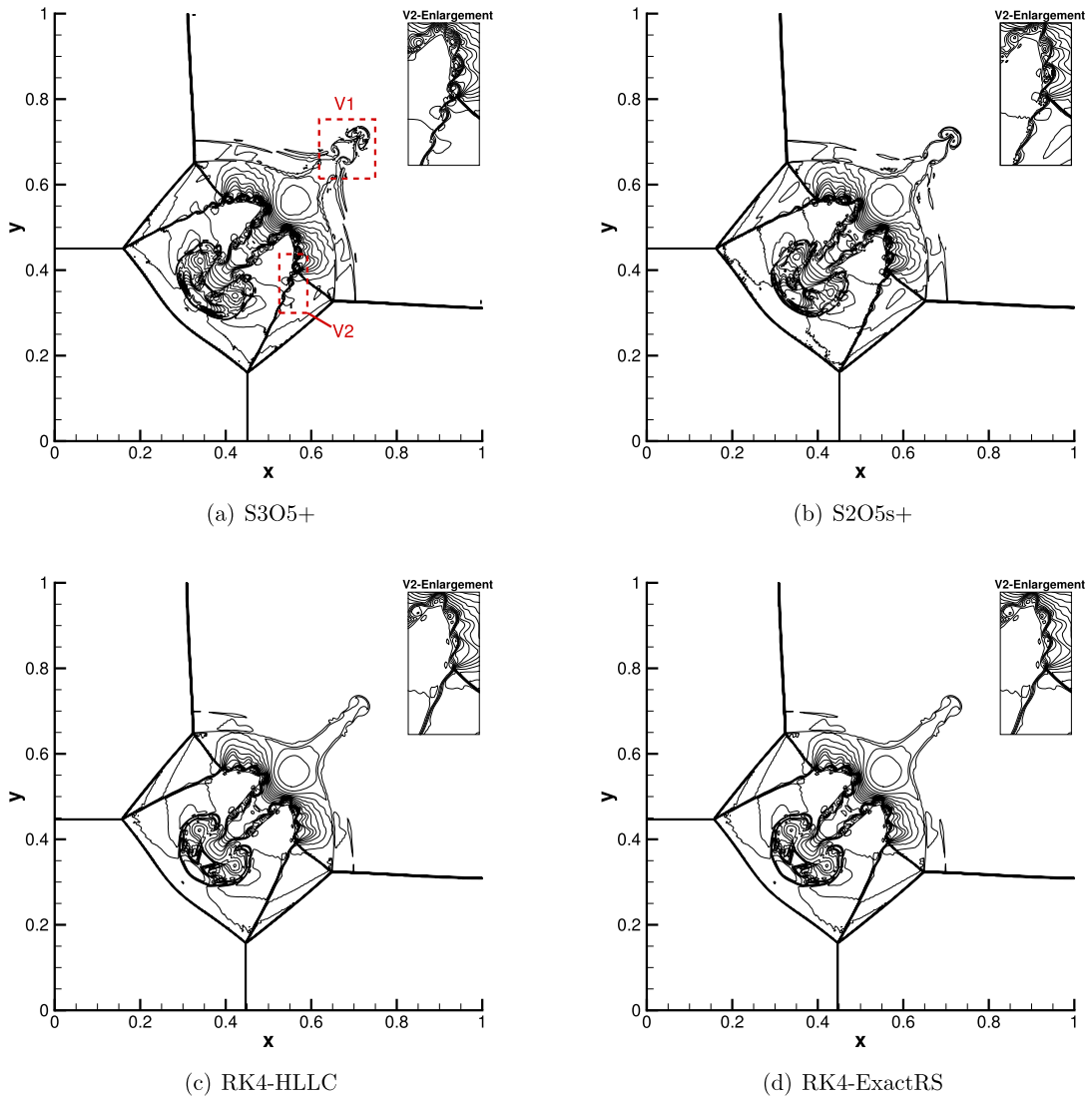


Fig. 8. The 23 equal-spaced density contours of Configuration 3 case in [25]. 500×500 mesh points are used in all calculations.

$$(\rho, u, v, p) = \begin{cases} (0.138, 1.206, 1.206, 0.029), & x < 0.7, y < 0.7, \\ (0.5323, 0, 1.206, 0.3), & x \geq 0.7, y < 0.7, \\ (1.5, 0, 0, 1.5), & x \geq 0.7, y \geq 0.7, \\ (0.5323, 1.206, 0, 0.3), & x < 0.7, y \geq 0.7. \end{cases}$$

At the output time $t = 0.6$, the same 23 density contours are plotted in Fig. 8 from different schemes. All schemes could capture the shock sharply. The main differences among all schemes are the strength of the shear layers, such as the V1 and V2 regions of Fig. 8(a). Both S3O5+ and S2O5s+ schemes could resolve the vortex pairs in V1 region better than those from the RK4 Riemann solvers based schemes. At the same time, gas kinetic schemes show stronger instabilities of the vortex sheets in V2 region.

(b2) Interaction of planar contact discontinuities

The Configuration 6 in [25] is tested. The initial condition in a square domain $[0, 2] \times [0, 2]$ is given by

$$(\rho, u, v, p) = \begin{cases} (1, -0.75, 0.5, 1), & x < 1, y < 1, \\ (3, -0.75, -0.5, 1), & x \geq 1, y < 1, \\ (1, 0.75, -0.5, 1), & x \geq 1, y \geq 1, \\ (2, 0.75, 0.5, 1), & x < 1, y \geq 1, \end{cases}$$

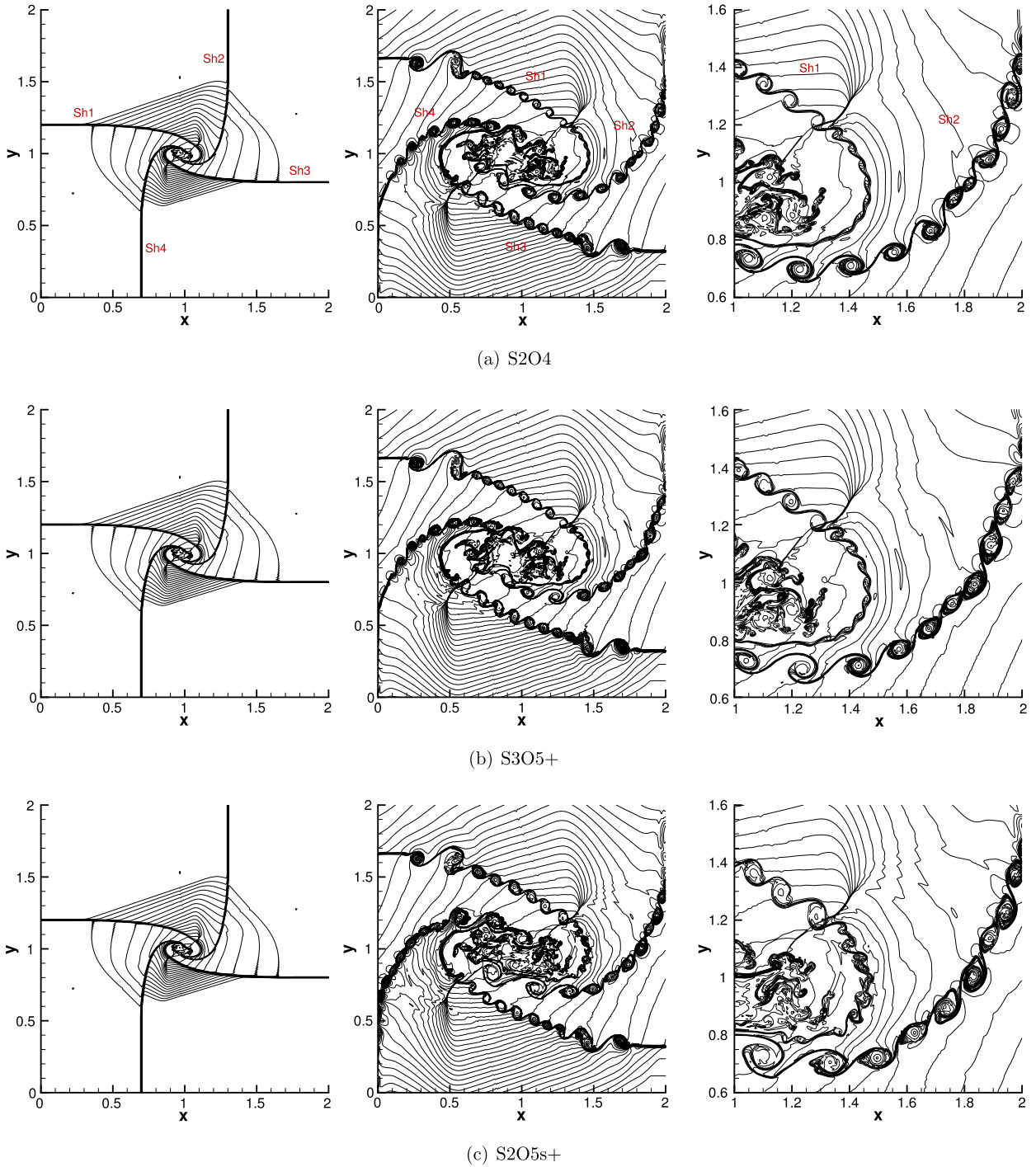


Fig. 9. The 40 equal-spaced density contours of Configuration 6 case in [25] by using multi-stage GKS. Left: $t = 0.4$. Middle: $t = 1.6$. Right: local enlargement density contours of middle figure. 800×800 mesh points are used in all calculations.

where four zones have different density and velocity, but the same pressure. Four shear layers will be formed by these planar contact discontinuity interactions. Similar to the isentropic vortex case, in order to reveal the influence of different time marching schemes a large domain $[0, 2] \times [0, 2]$ covered by 800×800 mesh points is used with the output times $t = 0.4$ and $t = 1.6$. The CFL condition is 0.5 in all calculations. As shown in the Fig. 9, at $t = 0.4$ the results from all schemes seem identical. However, at time $t = 1.6$, the flow structures become much more complicated. From the local enlargement of the central shear layer, the S2O4 and S3O5 schemes present more smaller vortexes, and the S2O5 scheme shows slightly less but a little bit larger size. In comparison with Riemann flux based RK4 Godunov method, as shown in

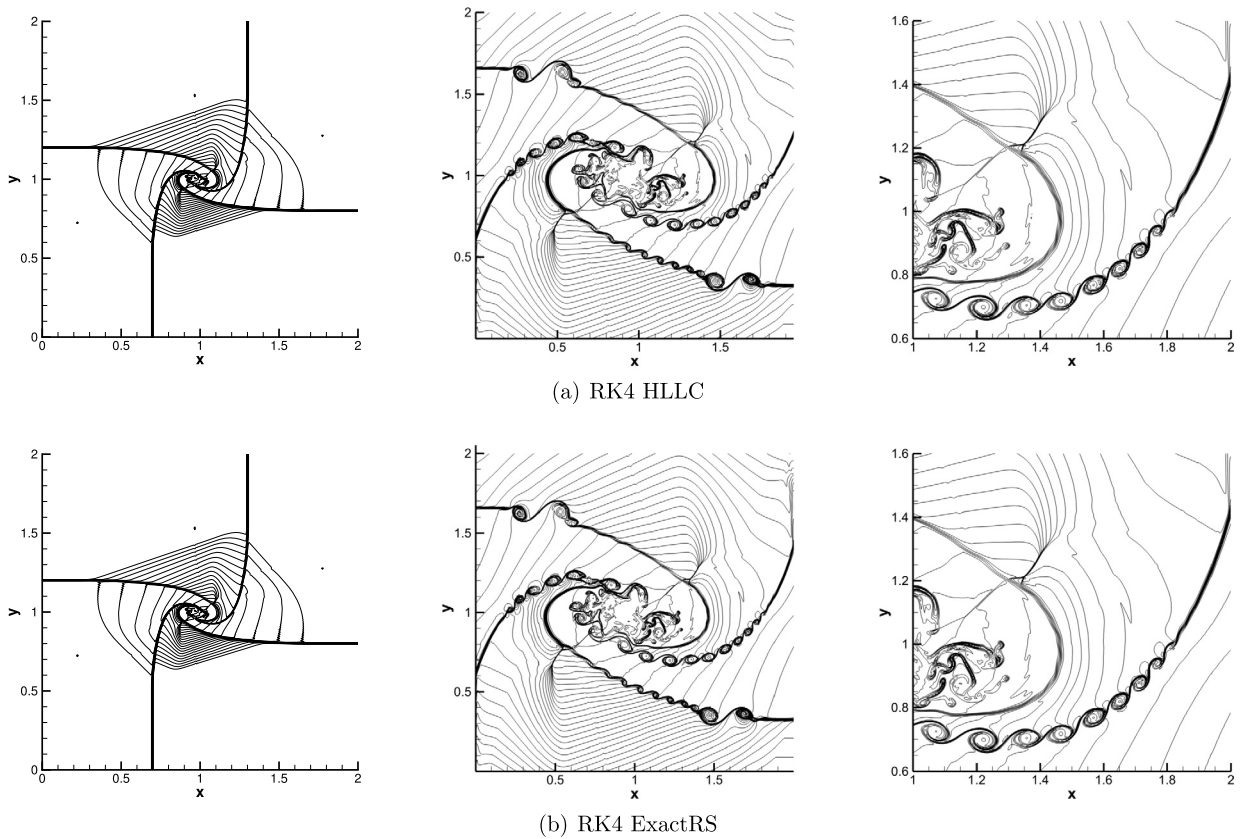


Fig. 10. The 40 equal-spaced density contours of Configuration 6 case in [25] by using RK4 Godunov methods. Left: $t = 0.4$. Middle: $t = 1.6$. Right: local enlargement of middle figure. 800×800 mesh points are used in all calculations.

Table 13

Computational time (in seconds) of different schemes for the 2D Riemann problem.

CPU time Mesh size	Schemes				
	S204	S205s+	S305+	RK5 HLLC	RK5 Exact-RS
100×100	7.640	8.057	10.959	6.028	20.223
200×200	26.309	45.551	46.801	24.022	80.880
300×300	58.524	94.102	94.523	53.833	171.647
400×400	102.985	138.153	158.364	94.293	292.566

Fig. 10, the traditional RK methods show more dissipative results than those from MSMD GKS. Different from GKS solutions, almost no instabilities for Sh1 wave are triggered for traditional RK4 methods. For Sh2 wave, both the number and the size of the vortices from RK4 Godunov methods are inferior in comparison with MSMD GKS results.

4.4. Computational efficiency

Based on the above 2D Riemann problem test case of interaction of planar contact discontinuities, the computational efficiency from different schemes will be evaluated. For S204, S305, S205 methods, the fluxes at three Gaussian points along a cell interface are needed, which are the same as RK5 Godunov scheme with Riemann flux. The 2D Riemann problem (Configuration 6 in [25]) with different mesh sizes are tested for the comparison of computation cost, which is shown in Table 13. The CPU times are recorded after running 10 time steps for each scheme with a single processor of Intel Xeon E5 2670 @2.60 GHz. Based on the table, the computational time of S305 GKS is about 1.5 times of S204 GKS due to the differences in number of stages. Another observation is that the computational speed for S205 and S305 is almost the same. However, for S205 scheme, only two stages of fluid variables are stored, which is less memory used than S305 scheme, but more computational time spent on the 3rd-order flux function.

The computational time for the traditional RK methods based on Riemann solvers is also obtained in Table 3. The RK5 method with HLLC flux seems faster than the S204 scheme. This is due to the simple HLLC flux function. The RK5 method with exact Riemann solver is almost two times more expensive than that of 5th-order GKS. But, even for the current 2D inviscid flow test case, the GKS always solves the Navier–Stokes (NS) equations. If RK5 Godunov type scheme is extended to

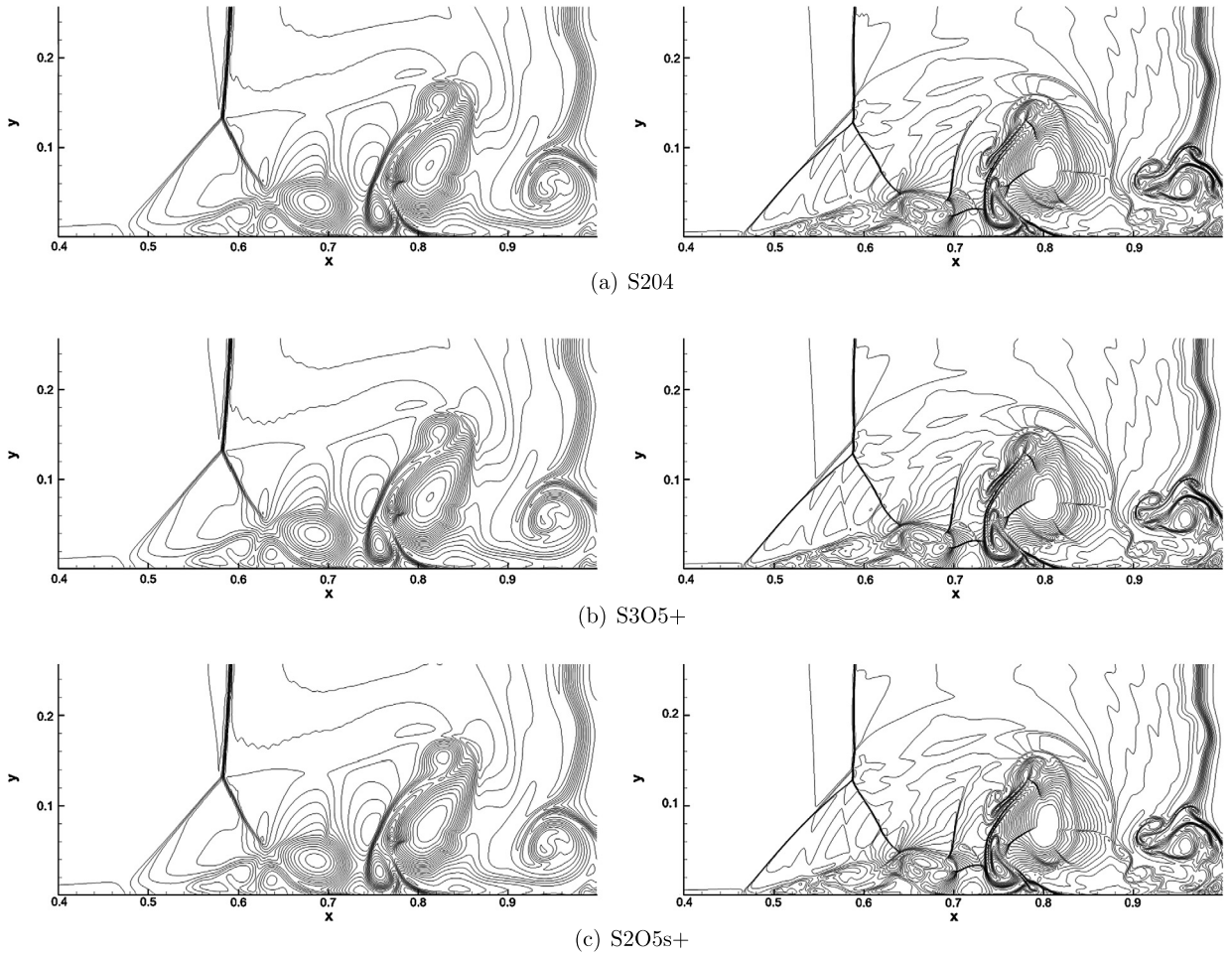


Fig. 11. The 21 equal-spaced density contours of viscous shock tube problems at $t = 1$ from different MSMD GKS. Left: $Re = 200$, 500×250 mesh points. Right: $Re = 1000$, 1000×500 mesh points.

solve the NS equations, the computational cost will at least be doubled, which will become inefficient in comparison with MSMD GKS. So, for the high order schemes and for the viscous flow computations, the design of high order time accurate flux solver is worthwhile.

4.5. Two dimensional viscous test cases

(a) Viscous shock tube problem under low Reynolds numbers

For N-S solvers, the viscous shock tube problem is a nice test case for the validity of the scheme due to the complicated flow structure and the shock boundary layer interaction [8]. The geometry is a two-dimensional unit box $[0, 1] \times [0, 1]$, with no-slip adiabatic walls. Two different constant conditions are given on both sides of $x = 0.5$,

$$(\rho, u, v, p) = \begin{cases} (120, 0, 0, 120/\gamma), & 0 < x < 0.5, \\ (1.2, 0, 0, 1.2/\gamma), & 0.5 \leq x < 1, \end{cases}$$

where $\gamma = 1.4$ and the Prandtl number $Pr = 0.73$. The computational domain is chosen as $[0, 1] \times [0, 0.5]$ due to the symmetry of the problem. The upper boundary is set as a symmetric boundary condition and the others boundaries are no-slip adiabatic condition. Two Reynolds number $Re = 200$ and 1000 are selected in the simulations. The results at $t = 1$ are presented. For such a low Reynolds number flow, the time step is determined by

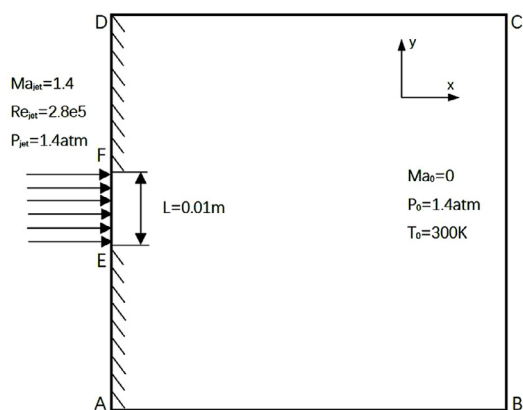
$$\Delta t = C_{CFL} \text{Min} \left(\frac{\Delta x}{|\sqrt{U^2 + V^2}| + a}, \frac{(\Delta x)^2}{4\nu} \right),$$

where C_{CFL} is the CFL number, a is the sound speed, and $\nu = \mu/\rho$ is the kinematic viscosity coefficient. The results from different GKS schemes are shown in Fig. 11. For both $Re = 200$ and 1000 , almost identical results are obtained from different schemes. The height of primary vortex for $Re = 200$ is shown in Table 14 [24].

Table 14

Heights of primary vortex from different schemes for $Re = 200$ and $\Delta x = \Delta y = 1/500$.

Schemes	AUSMPW+	M-AUSMPW+	S204
Height	0.163	0.168	0.173
Schemes	S205s+	S305+	
Height	0.174	0.173	



(a) Schematic of the computational domain

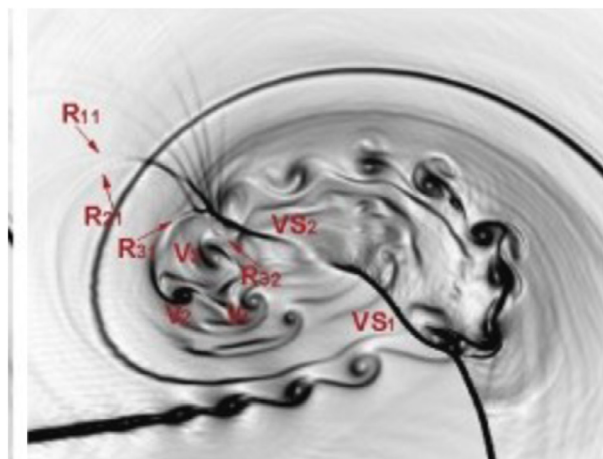
(b) Case 3 result at $t=0.15$ ms

Fig. 12. (a) The sketch of a planar jet case proposed in [52]. (b) The 2-D result without entrance perturbation in [52], at $t = 0.15$ ms. The numerical Schlieren-type images are plotted for visualization.

(b) A planar jet under high Reynolds number

Free supersonic jet flow is widely studied. A simplified 2-D planar jet, which was proposed by Zhang et al. [52], is used here to test high order GKS. A Mach 1.4 jet is injected through a width $L = 0.01$ m entrance into a square computational domain with the size $10L \times 10L$. The sketch of the geometry is plotted in Fig. 12(a). The Reynolds number is set as $Re_\infty = U_{jet}L/\nu = 2.8 \times 10^5$, and the dynamic viscosity coefficient $\nu = 1.73 \times 10^{-5}$ m²/s. The same mesh size of 1200×1200 as that in [52] is used here.

Fig. 13 shows the evolution process of the jet at three different output times $t = 0.08$ ms, 0.15 ms, and 0.32 ms. At $t = 0.08$ ms, the three schemes of S204, S305+, and S205s+, give almost identical results. At $t = 0.15$ ms, the jet structures from different schemes are similar, with small variations, such as the vortex sheets along the main shear layers due to the K–H instability. Current results can be compared with the one in Fig. 12(b), while the high order MSMD GKS seems present more clear flow structure, especially for the capturing of small size vortices. As the jet further develops up to $t = 0.32$ ms, significant differences in the shear layer and main vortex pairs could be observed from different schemes. The S205s+ scheme shows more distinct flow pattern in the center of vortex pairs. Fig. 13 provides abundant flow structures, such as shear layer instability, shock vortex interaction, and a wide range of vortex strength and sizes, which clearly demonstrate the power of high order schemes.

5. Conclusion

In this paper, a family of high order gas kinetic schemes with multi-stage multi-derivative techniques have been proposed, especially the two stages and three stages fifth-order schemes S205 and S305. Due to the use of time derivatives of the flux function, such as the second and third-order GKS time accurate flux functions, for the same temporal accuracy the current schemes can reduce the number of middle stages in comparison with the traditional Runge–Kutta methods, such as the RK5 method with the time independent Riemann flux. Therefore, the current MSMD GKS becomes more efficient than the RK methods, especially for the Navier–Stokes solutions. The high order MSMD GKS provides accurate numerical solutions for the compressible flows with the same robustness as the second-order methods in the flow simulations with strong shock interactions. The jet simulation provides the state-of-art numerical results from high order schemes.

The current MSMD gas kinetic schemes use the WENO type reconstruction for initial condition and spatial accuracy, which has a large stencils. Even though the MSMD GKS can be easily extended to unstructured mesh for the NS solutions, it is still preferred to develop high order compact gas kinetic schemes for the engineering applications with complicated geometry. As a continuation of the compact third-order GKS [34], the developments of the fourth-order and fifth-order compact schemes with the implementation of MSMD technique are under development.

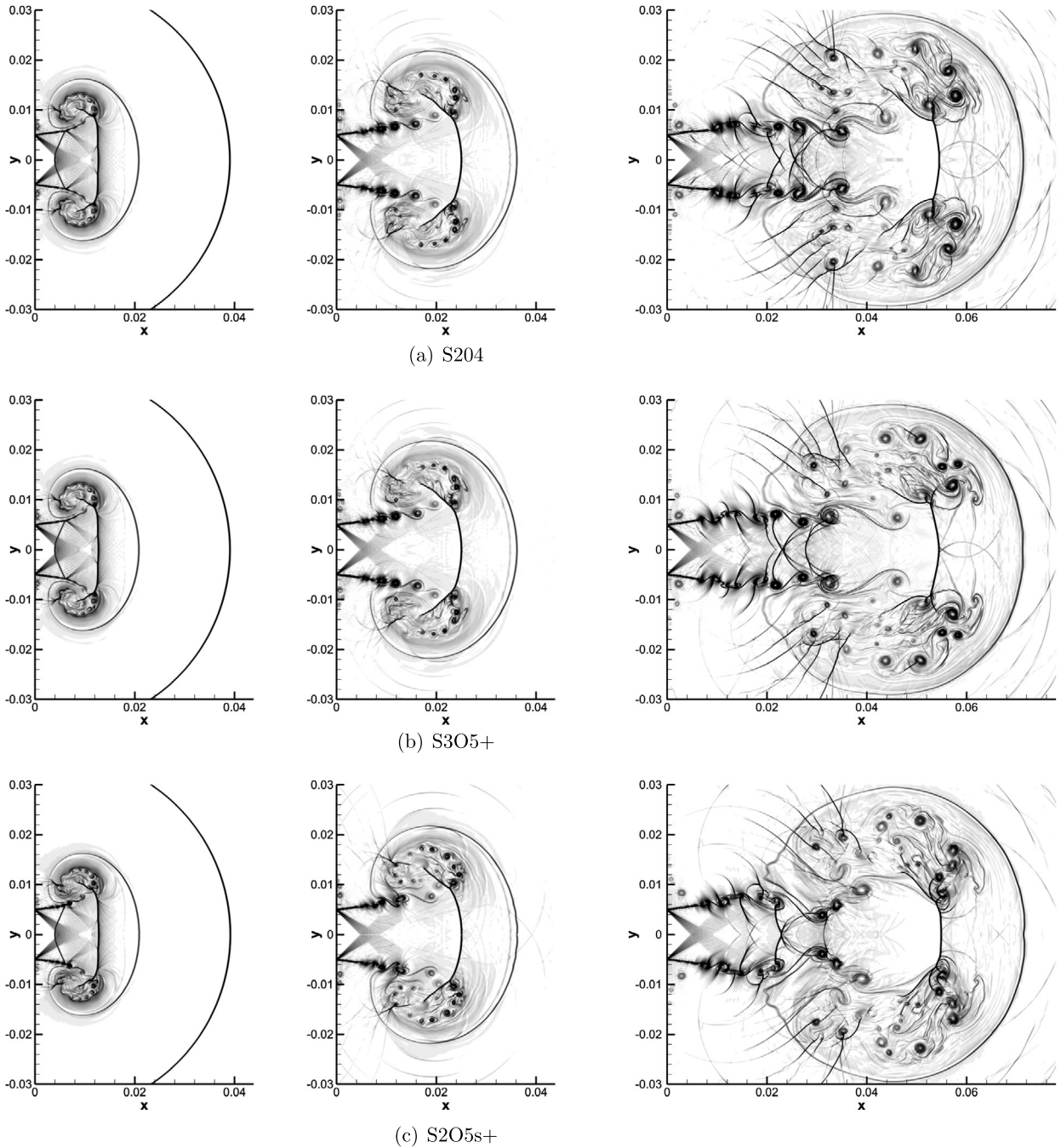


Fig. 13. The 2-D simulation of starting structures of Mach 1.4 planar jet under different MSMD GKS. Mesh size 1200×1200 . The Schlieren images by density gradient magnitude at $t = 0.08$ ms, 0.15 ms, 0.32 ms are given from left to right with 25 equidistant contours.

Acknowledgements

The authors would like to thank all reviewers for their constructive comments. The current work is supported by Hong Kong Research Grant Council (16211014, 16207715, 16206617), HKUST research fund (PROVOST13SC01, IRS16SC42, SBI14SC11), and National Science Foundation of China (91330203, 91530319, 11772281).

References

- [1] F. Acker, R.B. de R. Borges, Bruno Costa, An improved WENO-Z scheme, *J. Comput. Phys.* 313 (2016) 726–753.

- [2] Timothy J. Barth, Paul O. Frederickson, Higher order solution of the Euler equations on unstructured grids using quadratic reconstruction, *AIAA Pap.* 90 (1990) 0013.
- [3] Prabhu Lal Bhatnagar, Eugene P. Gross, Max Krook, A model for collision processes in gases, I: small amplitude processes in charged and neutral one-component systems, *Phys. Rev.* 94 (3) (1954) 511.
- [4] Rafael Borges, Monique Carmona, Bruno Costa, Wai Sun Don, An improved weighted essentially non-oscillatory scheme for hyperbolic conservation laws, *J. Comput. Phys.* 227 (6) (2008) 3191–3211.
- [5] Robert P.K. Chan, Angela Y.J. Tsai, On explicit two-derivative Runge–Kutta methods, *Numer. Algorithms* 53 (2) (2010) 171–194.
- [6] Andrew J. Christlieb, Sigal Gottlieb, Zachary Grant, David C. Seal, Explicit strong stability preserving multistage two-derivative time-stepping schemes, *J. Sci. Comput.* 68 (3) (2016) 914–942.
- [7] Bernardo Cockburn, Chi-Wang Shu, TVB Runge–Kutta local projection discontinuous Galerkin finite element method for conservation laws, II: general framework, *Math. Comput.* 52 (186) (1989) 411–435.
- [8] Virginie Daru, Christian Tenaud, Evaluation of TVD high resolution schemes for unsteady viscous shocked flows, *Comput. Fluids* 30 (1) (2000) 89–113.
- [9] Michael Dumbser, Olindo Zanotti, Raphaël Loubère, Steven Diot, A posteriori subcell limiting of the discontinuous Galerkin finite element method for hyperbolic conservation laws, *J. Comput. Phys.* 278 (2014) 47–75.
- [10] Yonglei Fang, Xiong You, Qinghe Ming, Trigonometrically fitted two-derivative Runge–Kutta methods for solving oscillatory differential equations, *Numer. Algorithms* 65 (3) (2014) 651–667.
- [11] Yonglei Fang, Yanwei Zhang, Ping Wang, Two-derivative Runge–Kutta methods with increased phase-lag and dissipation order for the Schrödinger equation, *J. Math. Chem.* (2017) 1–11.
- [12] Erwin Fehlberg, Low-Order Classical Runge–Kutta Formulas with Stepsize Control and Their Application to Some Heat Transfer Problems, NASA-TR-R-315, 1969.
- [13] Thomas B. Gatski, Jean-Paul Bonnet, Compressibility, Turbulence and High Speed Flow, Academic Press, 2013.
- [14] E. Gekeler, R. Widmann, On the order conditions of Runge–Kutta methods with higher derivatives, *Numer. Math.* 50 (2) (1986) 183–203.
- [15] Sigal Gottlieb, On high order strong stability preserving Runge–Kutta and multi step time discretizations, *J. Sci. Comput.* 25 (1) (2005) 105–128.
- [16] Sigal Gottlieb, Chi-Wang Shu, Eitan Tadmor, Strong stability-preserving high-order time discretization methods, *SIAM Rev.* 43 (1) (2001) 89–112.
- [17] Ernst Hairer, Gerhard Wanner, Multistep-multistage-multiderivative methods for ordinary differential equations, *Computing* 11 (3) (1973) 287–303.
- [18] F.Q. Hu, M.Y. Hussaini, J.L. Manthey, Low-dissipation and low-dispersion Runge–Kutta schemes for computational acoustics, *J. Comput. Phys.* 124 (1) (1996) 177–191.
- [19] H.T. Huynh, A flux reconstruction approach to high-order schemes including discontinuous Galerkin methods, *AIAA Pap.* 4079 (2007) 2007.
- [20] Satoshi Ii, Feng Xiao, High order multi-moment constrained finite volume method, part I: basic formulation, *J. Comput. Phys.* 228 (10) (2009) 3669–3707.
- [21] Antony Jameson, Wolfgang Schmidt, Eli Turkel, et al., Numerical solutions of the Euler equations by finite volume methods using Runge–Kutta time-stepping schemes, *AIAA Pap.* 1259 (1981) 1981.
- [22] Alexander Jaust, Jochen Schütz, David C. Seal, Implicit multistage two-derivative discontinuous Galerkin schemes for viscous conservation laws, *J. Sci. Comput.* 69 (2) (2016) 866–891.
- [23] Guang-Shan Jiang, Chi-Wang Shu, Efficient implementation of weighted ENO schemes, *J. Comput. Phys.* 126 (1) (1996) 202–228.
- [24] Kyu Hong Kim, Chongam Kim, Accurate, efficient and monotonic numerical methods for multi-dimensional compressible flows, part II: multi-dimensional limiting process, *J. Comput. Phys.* 208 (2) (2005) 570–615.
- [25] Peter D. Lax, Xu-Dong Liu, Solution of two-dimensional Riemann problems of gas dynamics by positive schemes, *SIAM J. Sci. Comput.* 19 (2) (1998) 319–340.
- [26] Jiequan Li, Zhifang Du, A two-stage fourth order time-accurate discretization for Lax–Wendroff type flow solvers, I: hyperbolic conservation laws, *SIAM J. Sci. Comput.* 38 (5) (2016) A3046–A3069.
- [27] Qibing Li, Kun Xu, Song Fu, A high-order gas-kinetic Navier–Stokes flow solver, *J. Comput. Phys.* 229 (19) (2010) 6715–6731.
- [28] Na Liu, Huazhong Tang, A high-order accurate gas-kinetic scheme for one-and two-dimensional flow simulation, *Commun. Comput. Phys.* 15 (4) (2014) 911–943.
- [29] Jun Luo, Kun Xu, A high-order multidimensional gas-kinetic scheme for hydrodynamic equations, *Sci. China, Technol. Sci.* 56 (10) (2013) 2370–2384.
- [30] N. Obreschkoff, Neue Quadraturforme, *Abh. K. Preuss. Akad. Wiss.* 4 (1940) 2–20.
- [31] Liang Pan, Jiequan Li, Kun Xu, A few benchmark test cases for higher-order Euler solvers, *Numer. Math. Theor. Meth. Appl.* 10 (4) (2017) 711–736.
- [32] Liang Pan, Kun Xu, A compact third-order gas-kinetic scheme for compressible Euler and Navier–Stokes equations, *Commun. Comput. Phys.* 18 (4) (2015) 985–1011.
- [33] Liang Pan, Kun Xu, A third-order gas-kinetic scheme for three-dimensional inviscid and viscous flow computations, *Comput. Fluids* 119 (2015) 250–260.
- [34] Liang Pan, Kun Xu, A third-order compact gas-kinetic scheme on unstructured meshes for compressible Navier–Stokes solutions, *J. Comput. Phys.* 318 (2016) 327–348.
- [35] Liang Pan, Kun Xu, Qibing Li, Jiequan Li, An efficient and accurate two-stage fourth-order gas-kinetic scheme for the Euler and Navier–Stokes equations, *J. Comput. Phys.* 326 (2016) 197–221.
- [36] Xiaodong Ren, Kun Xu, Wei Shyy, A multi-dimensional high-order DG-ALE method based on gas-kinetic theory with application to oscillating bodies, *J. Comput. Phys.* 316 (2016) 700–720.
- [37] Xiaodong Ren, Kun Xu, Wei Shyy, Chunwei Gu, A multi-dimensional high-order discontinuous Galerkin method based on gas kinetic theory for viscous flow computations, *J. Comput. Phys.* 292 (2015) 176–193.
- [38] Gustavo Franco Reynoso, Sigal Gottlieb, Zachary J. Grant, Strong stability preserving sixth order two-derivative Runge–Kutta methods, in: *AIP Conference Proceedings*, vol. 1863, AIP Publishing, 2017, p. 560068.
- [39] Jochen Schütz, David C. Seal, Alexander Jaust, Implicit multidervative collocation solvers for linear partial differential equations with discontinuous Galerkin spatial discretizations, *J. Sci. Comput.* 73 (2–3) (2017) 1145–1163.
- [40] David C. Seal, Yaman Güçlü, Andrew J. Christlieb, High-order multidervative time integrators for hyperbolic conservation laws, *J. Sci. Comput.* 60 (1) (2014) 101–140.
- [41] Hua-Zhong Tang, Kun Xu, A high-order gas-kinetic method for multidimensional ideal magnetohydrodynamics, *J. Comput. Phys.* 165 (1) (2000) 69–88.
- [42] Vladimir A. Titarev, Eleuterio F. Toro, ADER: arbitrary high order Godunov approach, *J. Sci. Comput.* 17 (1) (2002) 609–618.
- [43] Vladimir A. Titarev, Eleuterio F. Toro, Finite-volume WENO schemes for three-dimensional conservation laws, *J. Comput. Phys.* 201 (1) (2004) 238–260.
- [44] Vladimir A. Titarev, Eleuterio F. Toro, Ader schemes for three-dimensional non-linear hyperbolic systems, *J. Comput. Phys.* 204 (2) (2005) 715–736.
- [45] Eleuterio F. Toro, *Riemann Solvers and Numerical Methods for Fluid Dynamics: A Practical Introduction*, Springer Science & Business, Media, 2013.
- [46] Zhijian J. Wang, Krzysztof Fidkowski, Rémi Abgrall, Francesco Bassi, Doru Caraeni, Andrew Cary, Herman Deconinck, Ralf Hartmann, Koen Hillewaert, Hung T. Huynh, et al., High-order CFD methods: current status and perspective, *Int. J. Numer. Methods Fluids* 72 (8) (2013) 811–845.
- [47] Kun Xu, A gas-kinetic BGK scheme for the Navier–Stokes equations and its connection with artificial dissipation and Godunov method, *J. Comput. Phys.* 171 (1) (2001) 289–335.
- [48] Kun Xu, Xin He, Chunpei Cai, Multiple temperature kinetic model and gas-kinetic method for hypersonic non-equilibrium flow computations, *J. Comput. Phys.* 227 (14) (2008) 6779–6794.

- [49] Kun Xu, Juan-Chen Huang, A unified gas-kinetic scheme for continuum and rarefied flows, *J. Comput. Phys.* 229 (20) (2010) 7747–7764.
- [50] Kun Xu, Chang Liu, A paradigm for modeling and computation of gas dynamics, *Phys. Fluids* 29 (2) (2017) 026101.
- [51] Kun Xu, Meiliang Mao, Lei Tang, A multidimensional gas-kinetic BGK scheme for hypersonic viscous flow, *J. Comput. Phys.* 203 (2) (2005) 405–421.
- [52] Huanhao Zhang, Zhihua Chen, Xiaohai Jiang, Zhengui Huang, The starting flow structures and evolution of a supersonic planar jet, *Comput. Fluids* 114 (2015) 98–109.
- [53] Rui Zhang, Mengping Zhang, Chi-Wang Shu, On the order of accuracy and numerical performance of two classes of finite volume WENO schemes, *Commun. Comput. Phys.* 9 (3) (2011) 807–827.
- [54] Fengxiang Zhao, Liang Pan, Zheng Li, Shuanghu Wang, A new class of high-order weighted essentially non-oscillatory schemes for hyperbolic conservation laws, *Comput. Fluids* (2017).
- [55] Guangzhao Zhou, Kun Xu, Feng Liu, Simplification of the flux function for a high-order gas-kinetic evolution model, *J. Comput. Phys.* 339 (2017) 146–162.